Pickering emulsions based on food byproducts: A comprehensive study of soluble and insoluble contents

Delphine Huc-Mathis, Giana Almeida, C. Michon

Version of Record: https://www.sciencedirect.com/science/article/pii/S0021979720309590
Manuscript_cdccecfda3c7967df16d40b9dd1d3328

A mesoscale modelling approach of glass fibre/Elium Acrylic woven laminates for low velocity impact simulation

G. Kinvi-Dossou[1], N. Bonfoh[1*], R. Matadi Boumbimba[1], Y. Koutsawa[2], F. Lachaud[3], A. Nyoungue[4], P. Gerard[5]

[1]*Université de Lorraine, CNRS, Arts et Métiers Paris Tech, LEM3, F-57000 Metz, France**

[2]*Materials Research and Technology Department, Luxembourg Institute of Science and Technology, 5, rue Bommel, Z.A.E. Robert Steichen, L-4940 Hautcharage, Luxembourg.*

[3]*Institut Clément Ader (ICA), Université de Toulouse, CNRS - INSA - ISAE, 10 Avenue Edouard Belin, 31055 TOULOUSE Cedex 4, France.*

[4]*Université de Lorraine, LGIPM, F-57070 Metz, France*

[5]*ARKEMA, Groupement de Recherche de Lacq, F-64170 Lacq, France.*

Abstract

This study presents a numerical mesoscale approach to simulate the damage and failure mechanism of woven laminated composites under low velocity impact loading conditions. First, measurements were made on samples to obtain a realistic reproduction of the microstructure. This allows relating failure mechanisms in composite laminates with their geometry and topology. A three-dimensional Hashin criterion was developed to investigate the impact behaviour, by accounting for both intralaminar and interlaminar damage. Four failure modes were considered relatively to fibre damage initiation in tension and compression and Puck criteria was employed to capture the initiation of the yarn's matrix damage. The matrix surrounding undulated yarns were taken into account by an elastoplastic behaviour with maximum-stress failure criteria. Good correlation between numerical and experimental results demonstrated the robustness and the accuracy of the proposed multiscale approach.

* Corresponding author: Napo BONFOH
E-mail address: napo.bonfoh@univ-lorraine.fr

Keywords: A. Thermoplastic resin; A. Polymer-matrix composites (PMCs); B. Impact behaviour; C. Finite element analysis (FEA); Mechanics of Structure Genome (MSG)

1. Introduction

Fostered by the recyclability requirements and stringent environmental guidelines, the use of laminate composites based on thermoplastic resins is nowadays a challenge. In addition to the requirement for lighter vehicles to reduce CO2 emissions, car manufacturers have been constrained to widely use recyclable or reusable materials. Compliance with these new directives requires the development of existing thermoplastic resins or the implementation of new thermoplastic resins. To take advantage of the possibilities offered by thermoplastics and with a constant concern to protect the environment and the economy, Arkema had developed liquid acrylic thermoplastic resins able to polymerize at room temperature. In addition, obtaining laminated composites is through processes hitherto reserved for thermosetting (Infusion, RTM, Flex-moulding). These resins have improved thermomechanical properties compared to those of high diffusion polymers, such as polypropylene, with a lower heat resistance (about 60-100°C) than that of high performance polymers (PEEK, PPS, PEI) [1]. Among the thermoplastics used in automotive fields, polyamide resins reinforced with short fibres are more common and are used for parts under hood (injection ramps, cylinder head covers, intake manifolds, …). Their use for structural or semi-structural parts encounters obstacles related to their low rigidity. For long fibre laminate composites, the strength and rigidity of the structure come mainly from the fibres. Other reason for the barrier of thermoplastics matrix is their moderate melting temperature (between 200°C and 300°C) and their liquid state (most of them need to be heated to high temperature to polymerize). Aside from these limitations, thermoplastic resins are highly encouraged for the requirements of recyclability, weld ability and storage. Indeed, the thermoplastic granules can be stored indefinitely and at room temperature, while thermosets must be stored cold and for a limited

time if the resin and hardener are already mixed [2].

Few literature works are dedicated to the measurement and the modelling of mechanical properties of this new class of composites materials [1, 3]. Boufaida et al. [1, 4] studied the mechanical properties of laminated glass fibres/acrylic composite in terms of mesoscopic strain field analysis by combining a spectral solver and 3D-DIC (Digital Image Correlation) measurements. Despite the complex geometry and strong heterogeneities, the mechanical properties of these laminates composites can be determined by using numerical periodic homogenization technique [5, 6, 27]. Pini et al. [7, 8] reported that composite materials prepared by infusion with Elium and Elium impact (Elium filled with acrylic block copolymers at a nanometer scale) matrices depicted an intralaminar fracture toughness much higher than the one of neat Elium resin. The dependence of the fracture toughness of such composites on crack propagation velocity was observed to be slightly different from that of the relevant matrices. In a previous study [9], the enhancement of impact resistance of an acrylic based glass fibres laminate composite, by introducing acrylic copolymer blocks was investigated at different temperatures. The impact resistance of Elium Acrylic/glass fibre laminate composite was shown to increase when copolymers (Nanostrength) were added in the Elium matrix. The study of Bhudolia et al. [10] on the evaluation of fracture toughness of thin and thick ply Elium acrylic composite systems, showed a 30% and 70% interlaminar fracture toughness for thin ply/liquid MMA composite, compared to thick ply/liquid MMA and thin ply/epoxy composites respectively. Regarding the numerical aspects, many studies investigated the low velocity impact of woven composites [11-13]. Yang et al. [11] provided an experimental and numerical investigation of interply hybrid composites based on woven fabrics and PCBT resin subjected to low-velocity impact. The authors analysed the failure modes of the materials based on the damage morphology observed. Experimental and numerical investigations conducted by Llorca et *al.* [28] on hybrid nonwoven/woven

polyethylene 2D fabrics showed an enhancement of the energy absorption capability of these materials under ballistic impact loadings. Nevertheless, the ballistic performance was not significantly improved when using hybrid 3D woven pattern since the damage was concentrated around the impact zone in both cases [29].

Woven laminated composites are inherently multiscale structures and can be described at three levels: microscopic, mesoscopic and macroscopic scale. The microscopic scale corresponds to that of constituents (fibre and matrix), the mesoscopic scale consists of undulated yarns embedded in a resin and the macroscopic one represents the laminate obtained by superposition of the layers. Exploiting the multiscale nature of these structures by linking the different steps of heterogeneity and the equivalent homogeneous material allows to understand their complex behaviour. This makes it possible to refine the relationships between the different mechanisms of deformation and damage and to analyse the effects of each phase on the macroscopic behaviour [14]. By using an approximative but realistic description of triaxial braided composites, González et *al.* [30] reproduced the anisotropic tensile and non-linear behaviour of these materials by the means of a continuum damage model. Their model is based on the Hashin failure criteria to simulate the damage at the yarn's level and required a periodic boundary conditions on representative unit cell. Nevertheless, this modelling approach relies on the knowledge of the behaviour of the different phases at each level of heterogeneity. Most existing models rely on simplifying assumptions of the behaviour of local phases. In reality, woven laminates have a non-linear constitutive law at every scale, from material to structure. It therefore seems necessary to take into account the nonlinear behaviour of these materials to accurately predict their responses to impact loadings.

In this paper, numerical simulations of low velocity impact response of plain-woven glass laminated composites are carried out at the mesoscopic scale. A finite element method was

carried out in ABAQUS/Explicit using VUMAT user subroutine. The simulation results such as the impact resistance of the composites were compared with experimental data provided in [15]. Damage details in the impacted composite plates were obtained by the simulation and were analysed for different impact energies. The damage morphology was compared and led to more understanding the failure mechanisms of composite laminates under impact loading.

2. Material properties

The present study addresses a micromechanical approach to simulate the impact response of glass fibre reinforced (GFR) acrylic laminated composites. The considered material consists of a thermoplastic acrylic resin (ELIUM 150) with a low viscosity (150Cp) supplied by the company Arkema (GRL, France). This liquid resin was used to manufacture glass fibre reinforced composites. In addition to the acrylic monomer, this resin contains a peroxide catalyst to initiate the polymerization and an accelerator agent aimed at activating the peroxide catalyst. A hardener is used in a ratio of $0.345\ w/w$ (corresponding to $34.5\ g$ of hardener for $100\ g$ of resin). The woven glass fibres fabric was provided by CHOMARAT. The fibres fabric with a repeating length unit of $T = 7.8\ mm$, is a plain bi-directional woven fabric (taffetas) glass fibres, with a thickness of $T = 0.15\ mm$ and surface density of $600\ g/m^2$. The composite material was obtained by infusion process as detailed in [15, 16]. An experimental procedure described in the previous paper [16] provided some material data to feed the geometrical meso-model of the laminated composite. The Mechanics of Structure Genome (MSG) analysis is then performed to obtain anisotropic elastic properties of yarns.

2.1. Yarns effective elastic properties

Effective elastic properties of the composite yarns were computed from the first step of a multiscale approach based on the Mechanics of Structure Genome –MSG-, (see [16] and the references cited therein [5, 6, 17, 18]). The theory of MSG and its application to woven

composite modelling are discussed in Liu et al. [19]. In the jargon of MSG, the Structure Gene (SG) is the smallest mathematical building block of a structure and serves as the analysis domain within MSG. The SG can be a one-dimensional (1D), 2D or 3D domain depending on the microstructure of the composite structure. According to MSG, a homogenized model can be formulated by minimizing the loss of mechanical information between the original heterogeneous body and the homogeneous equivalent material. In the case of a linear elastic behaviour, this information can be the elastic strain energy density [16]. Hexagonal packing of 2-fibres and 8-fibres were considered regarding the topological texture revealed by MEB analysis. By assuming an isotropic elastic behaviour for each local phase, the authors computed the effective elastic properties as gathered in Table 1.

Table 1. Effective elastic properties of the composite Yarn

Young's modulus along fibre direction: E_{11} (GPa)	52.36
Transverse Young's modulus: E_{22}=E_{33} (GPa)	17.7
In-plane shear modulus: G_{23} (GPa)	6.377
Out of plane shear modulus: G_{13}=G_{12} (GPa)	6.155
Poisson's ratio: ν_{23}	0.387
Poisson's ratio : $\nu_{13} = \nu_{12}$	0.258

Prior to damage initiation, the transverse isotropic elastic behaviour of yarn is considered through the following orthotropic rigidity matrix:

$$\begin{pmatrix}\sigma_{11}\\ \sigma_{22}\\ \sigma_{33}\\ \sigma_{12}\\ \sigma_{31}\\ \sigma_{23}\end{pmatrix} = \begin{bmatrix} C_{11}^0 & C_{12}^0 & C_{13}^0 & & & \\ C_{12}^0 & C_{22}^0 & C_{23}^0 & & 0 & \\ C_{13}^0 & C_{11}^0 & C_{33}^0 & & & \\ & & & G_{12} & 0 & 0 \\ & 0 & & 0 & G_{31} & 0 \\ & & & 0 & 0 & G_{23} \end{bmatrix} \begin{pmatrix}\varepsilon_{11}\\ \varepsilon_{22}\\ \varepsilon_{33}\\ 2\varepsilon_{12}\\ 2\varepsilon_{31}\\ 2\varepsilon_{23}\end{pmatrix} \quad (1)$$

where:

$$C_{11}^0 = E_{11}^0(1-\nu_{23}\nu_{32})\Gamma, \qquad C_{22}^0 = E_{22}^0(1-\nu_{13}\nu_{31})\Gamma,$$

$$C_{33}^0 = E_{33}^0(1-\nu_{12}\nu_{21})\Gamma, C_{12}^0 = E_{11}^0(\nu_{21}+\nu_{31}\nu_{23})\Gamma, \tag{2}$$

$$C_{13}^0 = E_{11}^0(\nu_{31}+\nu_{21}\nu_{32})\Gamma, C_{23}^0 = E_{22}^0(\nu_{32}+\nu_{12}\nu_{31})\Gamma,$$

$$\Gamma = 1/(1-\nu_{12}\nu_{21}-\nu_{31}\nu_{13}-\nu_{23}\nu_{32}-2\nu_{21}\nu_{32}\nu_{13})$$

and E_{ij}^0 are the initial engineering constants of the undamaged yarn, as predicted by SG analysis.

In order to predict the damage of unidirectional yarns composite, Hashin [20] failure criteria modified by Puck (for the matrix failure) was considered. Since, only a 2D formulation of the Hashin criteria is available in Abaqus, its extension to a 3D configuration was developed and implemented in Abaqus/Explicit software as a user subroutine VUMAT.

2.2. Failure criteria of yarns fibre and matrix

The criterion considers four modes of failure: two for fibre (tension and compression) and two others for the matrix (tension and compression), as follows:

Fibre in tension ($\sigma_{11} \geq 0$) : $d_{f+} = \left(\frac{\sigma_{11}}{X_+}\right)^2 + \alpha\left(\frac{\sigma_{12}}{S_{12}}\right)^2 + \beta\left(\frac{\sigma_{13}}{S_{13}}\right)^2 = 1$ (3)

Fibre in compression ($\sigma_{11} < 0$) : $d_{f-} = \left(\frac{\sigma_{11}}{X_-}\right)^2 = 1$ (4)

Matrix : $d_m = \left(\frac{\sigma_{11}}{2X_+}\right)^2 + \frac{(\sigma_{22}+\sigma_{33})^2}{Y_+Y_-} + \left(\frac{\sigma_{12}}{S_{12}}\right)^2 + (\sigma_{22}+\sigma_{33})\left(\frac{1}{Y_+}+\frac{1}{Y_-}\right) = 1$ (5)

where $d_m = d_{m+}$ in tension ($\sigma_{22}+\sigma_{33} \geq 0$) and $d_m = d_{m-}$ in compression ($\sigma_{22}+\sigma_{33} <$

0).

$X_{(+/-)}, Y_{(+/-)}$, S_{12} and S_{13} are respectively the maximum tensile stress along the longitudinal, transverse and shear directions (Table 2). $d_{f(+/-)}\ et\ d_{m(+/-)}$ are the damage variables associated to the four failure modes. Coefficients $\alpha\ et\ \beta$ are related to shear contribution (respectively in the planes (1,2) and (1,3)) to fibre damage initiation in tension. The fibres are assumed to be uniaxially oriented along direction 1.

Table 2. Strengths of the yarns (fibre volume fraction: 70%)

Parameters	**X_+** (GPa)	**X_-** (GPa)	**Y_+** (GPa)	**Y_-** (GPa)	**$S_{12} = S_{13}$** (GPa)
	3.95	3.45	0.485	0.49	0.298

2.3. Yarns damage model

Once damage initiates inside yarn, the response elastic response of the damaged yarns reads:

$$\begin{pmatrix}\sigma_{11}\\ \sigma_{22}\\ \sigma_{33}\\ \sigma_{12}\\ \sigma_{31}\\ \sigma_{23}\end{pmatrix} = \begin{bmatrix} C_{11}^d & C_{12}^d & C_{13}^d & & & \\ C_{12}^d & C_{22}^d & C_{23}^d & & 0 & \\ C_{13}^d & C_{11}^d & C_{33}^d & & & \\ & & & C_{44}^d & 0 & 0 \\ & 0 & & 0 & C_{55}^d & 0 \\ & & & 0 & 0 & C_{66}^d \end{bmatrix} \begin{pmatrix}\varepsilon_{11}\\ \varepsilon_{22}\\ \varepsilon_{33}\\ \varepsilon_{12}\\ \varepsilon_{31}\\ \varepsilon_{23}\end{pmatrix} \tag{6}$$

where:

$$C_{11}^d = (1-d_f)C_{11}^0, \qquad C_{22}^d = (1-d_f)(1-d_m)C_{22}^0,$$
$$C_{33}^d = (1-d_f)(1-d_m)C_{33}^0, C_{12}^d = (1-d_f)(1-d_m)C_{12}^0, \tag{7}$$

$$C_{13}^{d} = \left(1 - d_f\right)(1 - d_m)C_{13}^{0}, C_{23}^{d} = \left(1 - d_f\right)(1 - d_m)C_{23}^{0},$$

$$C_{44}^{d} = 2\left(1 - d_f\right)(1 - S_{m+}d_{m+})(1 - S_{m-}d_{m-})G_{12},$$

$$C_{55}^{d} = 2\left(1 - d_f\right)(1 - S_{m+}d_{m+})(1 - S_{m-}d_{m-})G_{13},$$

$$C_{66}^{d} = 2\left(1 - d_f\right)(1 - S_{m+}d_{m+})(1 - S_{m-}d_{m-})G_{23}$$

d_m et d_f are global damage variables respectively of the matrix and the fibre as:

$$\begin{aligned} d_m &= 1 - (1 - d_{m+})(1 - d_{m-}) \\ d_f &= 1 - (1 - d_{f+})(1 - d_{f-}) \end{aligned} \tag{8}$$

$S_{m(+/-)}$ is a factor that controls the shear modulus loss caused by matrix failure in tension or compression. Empirically, as in [21] these parameters are set at $S_{m+} = 0.8$ and $S_{m-} = 0.5$. A variable is introduced in the developed routine to facilitate the deletion of elements whose damaged stiffness matrix is reduced to 0. The progressive damage (softening) was not considered due to the brittle fracture of the yarns.

2.4. Pure matrix elastoplastic behaviour

Elium Acrylic mechanical behaviour can be assumed similar to poly-methyl-methacrylate (PMMA) [1, 22]. To describe the inelastic behaviour of the acrylic matrix, we adopted the model suggested by Nasraoui [23] that takes into account the temperature, the strain deformation and the hydrostatic pressure. This model is based on the work of G'Sell-Jonas [24] and assumed a combination of an additive and multiplicative formulation. Within this model, the yield stress is described by the following equation:

$$\sigma_y(\theta,\varepsilon,\dot{\varepsilon}) = \left[1-\frac{\theta}{T_g}\right][1-\exp(-w\varepsilon)]\left[\sigma_1\exp(-b\varepsilon)\left(\frac{\dot{\varepsilon}}{\dot{\varepsilon}_0}\right)^{m_1} + \sigma_2\exp\left[\left(h_0+h_1\frac{\theta-T_{ref}}{T_{ref}}\right)\varepsilon^2\right]\left[1+\left(\frac{\dot{\varepsilon}}{\dot{\varepsilon}_0}\right)^{-1}\right]^{-m_2}\right] \quad (9)$$

where T_{ref} stands for the reference temperature (298 K) and $\dot{\varepsilon}_0$ the reference strain rate. The parameters $\sigma_1, \sigma_2, h_0, h_1, w, b$ are intrinsic to the material and were identified by Nasraoui [23] for PMMA through quasi-static and dynamic compression tests using Hopkinson bar system. Nasraoui's model [23] provides a good agreement between the experimental results and the predictions. It also enables to simulate the transition between elastic and hardening zones. In addition, this model exhibits a good flexibility for describing the inelastic behaviour of PMMA over a wide range of strain rate and temperature. Parameters identified for this model are summarized in Table 3. The flowchart for numerical integration of the material law using an explicit scheme is summarized in Fig. 2.

Table 3. Parameters for Nasraoui [23] model identified by compression test on PMMA

T_g(K)	σ_1(MPa)	σ_2(MPa)	h_0(-)	h_1(-)	m_1(-)	m_2(-)	w(-)	b(-)	$\dot{\varepsilon}_0$ (s^{-1})
378	1550	605	0.9	1.655	0.125	0.071	14.079	12.09	0.1

2.5. Cohesive zones model

In order to simulate the interlaminar delamination of the laminated composites subjected to low velocity impact, a cohesive zone model was considered. In addition to the penalty stiffness, these models require defining an initiation criterion for the crack initiation and a propagation criterion based on energy considerations. The criterion adopted for the interlaminar damage initiation is a traction-separation law:

$$\left(\frac{\sigma_n}{N}\right)^2 + \left(\frac{\sigma_t}{T}\right)^2 + \left(\frac{\sigma_s}{S}\right)^2 = 1 \quad (10)$$

where σ_n, σ_t, σ_s are respectively the tensile stress relatively to the normal direction n and shear directions s and t. N, T and S stand for their critical values. The delamination propagation is predicted under a mixed mode loading based on the Benzeggagh-Kenane (B-K) energy criterion [25]

$$G_C = G_{IC} + (G_{IIC} - G_{IC}) \cdot \left(\frac{G_{II} + G_{III}}{G}\right)^{\eta} \quad (11)$$

$G = G_I + G_{II} + G_{III}$ refers to the total energy release rate. $\eta = 1.45$ is the B-K parameter determined from the experimental data of a mixed mode delamination test. In [16], double cantilever beam (DCB) and end notched flexure (ENF) samples were tested according to the ASTM D5528 standard in order to characterize the fracture toughness of the composite laminates.

Table 4. Initial stiffness of the interface, damage initiation and propagation parameters

Initial stiffness (MPa/mm)			**Interlaminar strength (MPa)**			**Fracture toughness (N/mm)**		
Mode I	Mode II	Mode III	Mode I	Mode II	Mode III	Mode I	Mode II	Mode III
Kn	Kt	Ks	N	T	S	G_{IC}	G_{IIC}	G_{IIIC}
175000	175000	175000	70	80	80	1.88	3.84	3.84

The use of the judicious cohesive model is crucial since it can lead to compliance difficulty and wrong results. DCB test as described in [16] has been numerically simulated in order to identify values of the interfacial stiffness and strength. A 3D model was therefore built via ABAQUS/Explicit software using an explicit time integration rule.

The developed numerical model consists of an assembly of two half-beams of $165mm \times$

$25mm \times 1{,}7mm$. These beams are meshed with 6000 C3D8R elements separated by a very small distance (0.001 mm) as cohesive zone. A cohesive behaviour was then introduced as an interaction between the nodes of the two opposite surfaces while guaranteeing the pre-crack length of $a_0 = 40\ mm$. All the parameters used in the cohesive zone model are summarized in Table 4. The elastic properties of the orthotropic plies were computed from the second step of the multiscale approach detailed in [16].

Table 5. Arms elastic properties used in the DCB model

$E_1 = E_2$ (GPa)	E_3 (GPa)	$G_{23} = G_{13}$ (GPa)	G_{12} (GPa)	$\nu_{23} = \nu_{13}$	ν_{12}
22.730	10.70	2.92	3.89	0.377	0.150

The fracture toughness of the laminates is given in Table 5 as well as the values adopted for the penalty stiffness and the strength of the interface. The penalty stiffness is chosen high to guarantee a quasi-rigid connection between adjacent plies, as suggested by Lachaud et *al.* [26]. Comparison of the DCB test results with the experimental data allow to validate the penalty stiffness which correctly reproduces the initial slope of the force versus displacement curve. Then, the model cohesive zone, with these parameters, was used to simulate the delamination in the laminates subjected to low velocity impact loadings.

3. Low velocity impact tests and finite element modelling

The present study aims to propose a numerical modelling of the low velocity impact and damage of textile composite materials at the mesoscale. To test the relevance of the developed model, its predictions were then compared with some experimental data [15].

3.1. Low velocity impact tests

Low velocity impact tests were performed on an Instron drop weight tower following the ASTM D7136, by varying the impact energy from 10J to 60J, at ambient temperature (20°C).

The total mass of the impactor and the drop system attached is 5.632 kg. The hemispherical impactor of $16\,mm$ diameter houses an accelerometer. The device is instrumented with a photocell able to measure the impactor velocity just before the impact and with an anti-rebound system that avoid multiple impacts. The composite plates of $100\text{mm} \times 150\text{ mm} \times 2\text{mm}$ were fixed on a rectangular support using four rubber-tipped clamps. The lower rigid support's opening measures $75\text{ mm} \times 125\text{ mm}$. Different graphs such as force versus displacement and energy versus time were plotted. In the next section, a geometrical description of the laminated plate at a mesoscale and the finite elements model are presented.

3.2. Finite elements modelling

A numerical model was developed to well describe the damage process of woven laminate composite plates subjected to low velocity impact. It is proposed to generate a model able to predict damage and failure on a more realistic geometry.

- **Geometry**

At the mesoscale, a realistic geometry of the laminate composite plates has been created thanks to Texgen software. This software can highlight the architecture of the yarns embedded in the acrylic matrix (Fig. 4). To this end, some tomographic analysis of the laminate as reported by Fig. 1 were analysed. The section shape of fibres tow are considered elliptic with a major diameter and minor diameter of 3.47 mm and 0.22 mm respectively (Fig. 5). A single layer is reproduced using Texgen and duplicated to obtain a 4-layers laminate samples.

- **Boundary conditions and meshing**

In order to reduce the number of elements, only a quarter of the plate was modelled. Each layer was meshed with $37\,500$ voxels (Fig. 6). The total number of elements in the model was 151568 including 150000 for the composite plate. A 3D element type (C3D8R) was used for the matrix and the yarns. The fixation conditions with four rubber-tipped clamps as described

in Section 3.1. have been considered. Due to the presence of rubber, the contact effort is poorly controlled during solicitations. We decide to replace the rigid fixer by a fixation of $5\,\text{nodes} \times 5\,\text{nodes}$ around the contact point. A frictionless tangential behaviour was considered, and a general contact was defined to avoid element interpenetration after the delamination occurs. Note that the interlaminar delamination was introduced using cohesive contact properties between adjacent layers.

Numerical simulations were performed for a time period of $15\,ms$ on a computer equipped with 36 cores (in parallel on Intel (R) Xeon (R) CPU E5-2640 v4 workstations, 2 × 2.40 GHz and 64 GB RAM). Impact energies ranging from 10J to 50J were tested. Due to the complexity of the modelled geometry, we considered small thickness of finite elements that generates a relatively small stable time increment of $10^{-9}\,s^{-1}$. After a convergence analysis, a time increment of about $10^{-8}\,s^{-1}$ was selected. In case of convergence difficulty, induced by high non-linearity, this increment was automatically reduced to $10^{-9}\,s^{-1}$.

4. Results and discussion

In this section, we present some results of the low velocity impact tests as predicted by the developed numerical modelling and the comparison with experimental data. This comparison was performed as well for the global response (force versus time, displacement versus time and energy versus time) as for damage process.

4.1. Macroscopic response

Fig. 7(a) and (b) depict respectively the force and energy as function of time, for an impact energy of 10J. Similarly, Fig. 7(c) and (d) are related to an impact energy of 20 J.

Compared with experimental data, the impact energy and forces are well predicted by the numerical model. However, it is worth noting an overestimation of the critical force (F_{max}) during numerical simulations. At 10J, the difference between the predicted and experimental

critical forces is about 9.3 %. This relative difference increases to 19% at 20J. This divergence between experimental and numerical results is also noticed for absorbed energies. Indeed, the absorbed energy predicted by the numerical simulation appears weak, compared with experimental data.

At 10 J, numerical results appeared in agreement with the experimental displacement of the impactor, as depicted by Fig. 8. Numerical values of the maximum deflection and the corresponding time still lower than experimental results. At $t = 6\,ms$, a maximal displacement of $7.73\,mm$ is numerically predicted and is $0.27\,mm$ less than corresponding experimental data (Figure 4 (b)).

At impact energy of 30 J and 40 J, numerical predictions are more relevant (Fig. 9 and Fig. 10). Trends of force and impact energy versus time curves are correctly reproduced. One can notice that the critical force and absorbed energy are close to the experimental results. For the absorbed energy, the relative difference remains less than 7%.

Despite this similarity, the effort drops more rapidly in the numerical model. This could be related to the loss of stiffness that results from element deletion introduced in the numerical model. In addition, oscillations in the force curves synchronize well with the experimental ones. The area under the force-versus-displacement curve corresponds to the energy absorbed by the material and dissipated during damage process (Fig. 10).

Regarding the maximum displacement at 30 J, the trend is reversed. At $t = 6\,ms$ and for an impact energy of 30 J, the maximum displacement is 12.25 mm and is slightly higher than the experimental one. The fibre damage seems more marked than what the experimental observations reveal. This contrast with respect to 10 J and 20 J may be due to the sensitivity of failure stresses. Indeed, all the simulations were performed considering the same values of maximum stresses relatively to the failure modes. That can be debatable since the strain rate varies at different impact energies.

By analysing the distribution of the displacement fields around the impactor (Fig. 11), we noticed the displacement increases with the energy. When the time or the energy increases, we are witnessing a lifting of the lateral edges of the plate as it was the case experimentally, due to considered clamping conditions. At 50 J and for $t = 6\,ms$, a total penetration of the plate was observed. This also explains the elastic springback of the plate (Fig. 11d). This penetration is partially due to the fact that at this impact energy, the deleted elements in the model no longer contribute to the stiffness of the damaged composite plate. At high impact energy, the friction behaviour between the plate and impactor and the mechanism of adiabatic self-heat have to be considered in order to improve the numerical predictions. It's also well-known that the loading rate influences the fracture toughness of the laminated composites [26].

Under the impactor, a cross-fracture surface was identified due to the geometry of the laminate. Damage by tension occurs first in the fibres near to the opposite face to that impacted. A successful correlation was made between the cross section of the central area of the numerical model and tomographic image of the damaged plate at 60 J. The indentation due to the impact loading at 60 J is $10.34\,mm$ during experiments and about $9\,mm$ for numerical simulation.

4.2. Intralaminar and interlaminar damage

The yarn's matrix damage based on the puck criterion is illustrated in Fig. 13. This figure revealed that the matrix cracking is initiated near the ply opposite to that in contact with the impactor. When the time increases, the delamination gradually propagates in the direction ± 45 °. We have also highlighted from the simulation results that clamping points are sensitive to matrix cracking. In other hand, delaminations have been simulated by the surface-based cohesive connection. Adjacent surfaces were considered in pairs as shown in Fig. 14. Results revealed that the delaminated area decreases gradually from the top to the bottom of the plate

and increases with the impact energy. Furthermore, we noticed that the direction of propagation is the same for all plies.

5. Conclusions

We proposed a finite elements-based model for the simulation of low-velocity impact response of taffeta woven laminates. To this end, an Abaqus/Explicit VUMAT user subroutine have been developed to integrate the elastic-damage behaviour of yarns embedded in an elastoplastic matrix. The goal of this approach was to take into account the effect of the woven topology and nonlinear behaviour on the damage patterns. In return, a refined mesh was required and therefore, only a quarter of the laminated plate was modelled due to the macro-isotropic feature of the plate. A key point of the developed approach is its ability to predict more efficiently and more accurately the macroscopic response and localized fields in each local phase of the heterogeneous material. Performed numerical simulations revealed a good agreement in comparison with experimental results available in [1]. Moreover, predicted results indicated that the delamination at interfaces were correctly described by a surface-based cohesive behaviour. By comparing the predictions for different impact energies, we can also highlight that a strain rate dependent behaviour may be considered.

Acknowledgments

We would like to acknowledge the fruitful discussions that we have had between the co-authors of this manuscript with a particular gratitude to the IRT-M2P which provides resources.

6. References

[1] Boufaida Z, Farge L, André S, Meshaka Y. Influence of the fiber/matrix strength on the mechanical properties of a glass fiber/thermoplastic-matrix plain weave fabric composite. Composites Part A: Applied Science and Manufacturing. 2015;75:28-38.

[2] http://www.arkema.fr/fr/produits/product-finder/range/Resines-Elium/.

[3] Pini T, Briatico Vangosa F, Frassine R, Rink M. Fracture toughness of acrylic resins: Viscoelastic effects and deformation mechanisms2018.

[4] Bashar M, Sundararaj U, Mertiny P. Microstructure and mechanical properties of epoxy hybrid nanocomposites modified with acrylic tri-block-copolymer and layered-silicate nanoclay. Composites Part A: Applied Science and Manufacturing. 2012;43:945-54.

[5] Liu X, Rouf K, Peng B, Yu W. Two-step homogenization of textile composites using mechanics of structure genome. Composite Structures. 2017;171:252-62.

[6] Yu W, Tang T. Variational asymptotic method for unit cell homogenization. Solid Mechanics and its Applications. 2010;168:117-30.

[7] Pini T. Fracture behaviour of thermoplastic acrylic resins and their relevant unidirectional carbon fibre composites: rate and temperature effects2017.

[8] Pini T, Caimmi F, Briatico-Vangosa F, Frassine R, Rink M. Fracture initiation and propagation in unidirectional CF composites based on thermoplastic acrylic resins. Engineering Fracture Mechanics. 2017;184:51-8.

[9] Matadi Boumbimba R, Coulibaly M, Khabouchi A, Kinvi-Dossou G, Bonfoh N, Gerard P. Glass fibres reinforced acrylic thermoplastic resin-based tri-block copolymers composites: Low velocity impact response at various temperatures. Composite Structures. 2017;160:939-51.

[10] Bhudolia SK, Perrotey P, Joshi SC. Mode I fracture toughness and fractographic investigation of carbon fibre composites with liquid Methylmethacrylate thermoplastic matrix. Composites Part B: Engineering. 2018;134:246-53.

[11] Yang B, Wang Z, Zhou L, Zhang J, Liang W. Experimental and numerical investigation of interply hybrid composites based on woven fabrics and PCBT resin subjected to low-velocity impact. Composite Structures. 2015;132:464-76.

[12] Chen Z, Yang F, Meguid SA. Multi-level modeling of woven glass/epoxy composite for multilayer printed circuit board applications. International Journal of Solids and Structures. 2014;51:3679-88.

[13] Xu Z, Yang F, Guan Z, Cantwell WJ. An Experimental and Numerical Study on Scaling Effects in the Low Velocity Impact Response of CFRP Laminates. Composite Structures. 2016;154:69-78.

[14] Zhou J, Guan Z, Cantwell W. Numerical modelling of perforation impact damage of fibre metal laminates. 2014:1-12.

[15] Kinvi-Dossou G, Matadi Boumbimba R, Bonfoh N, Garzon-Hernandez S, Garcia-Gonzalez D, Gerard P, et al. Innovative acrylic thermoplastic composites versus conventional composites: Improving the impact performances. Composite Structures. 2019;217:1-13.

[16] Kinvi-Dossou G, Boumbimba RM, Bonfoh N, Koutsawa Y, Eccli D, Gerard P. A numerical homogenization of E-Glass/Acrylic woven composite laminates: application to low velocity impact. Composite Structures. 2018.

[17] Peng B, Goodsell J, Byron Pipes R, Yu W. Generalized Free-Edge Stress Analysis Using Mechanics of Structure Genome. Journal of Applied Mechanics. 2016;83:101013--7.

[18] Koutsawa Y, Belouettar S, Makradi A, Tiem S. X-FEM implementation of VAMUCH: Application to active structural fiber multi-functional composite materials. Composite Structures. 2012;94:1297-304.

[19] Liu X, Yu W. A novel approach to analyze beam-like composite structures using mechanics of structure genome. Advances in Engineering Software. 2016;100:238-51.

[20] Hashin Z. Failure Criteria for Unidirectional Fiber Composites. Journal of Applied Mechanics. 1980;vol. 74:pp. 329-34.

[21] Nie Z. Advanced Mesomechanical Modeling of Triaxially Braided Composites for Dynamic Impact Analysis With Failure. 2014.

[22] Boufaida Z, Boisse J, André S, Farge L. Mesoscopic strain field analysis in a woven composite using a spectral solver and 3D-DIC measurements. Composite Structures. 2017;160:604-12.

[23] Nasraoui M, Forquin P, Siad L, Rusinek A. Influence of strain rate, temperature and adiabatic heating on the mechanical behaviour of poly-methyl-methacrylate: Experimental and modelling analyses. Materials and Design. 2012;37:500-9.

[24] G'Sell C, Jonas J. Determination of the plastic behaviour of solid polymers at constant true strain rate1979.

[25] Lou X, Cai H, Yu P, Jiao F, Han X. Failure analysis of composite laminate under low-velocity impact based on micromechanics of failure. Composite Structures. 2017;163:238-47.

[26] Ilyas M, Lachaud F, Espinosa C, Michel L, Salaün M. Modélisation en dynamique rapide du délaminage des composites à l'aide d'éléments finis cohésifs: "Dynamic delamination modeling of unidirectional composites by cohesive finite elements". 16th national day on composite materials (JNC -16), June 10-12, 2009, Toulouse, France.

[27] S. Sádaba, M. Herráez, F. Naya, C. González, J. Llorca, C.S. Lopes, Special-purpose elements to impose Periodic Boundary Conditions for multiscale computational homogenization of composite materials with the explicit Finite Element Method, Composite Structures, 2019;vol. 208:pp. 434-441.

[28] F. Martínez-Hergueta, A. Ridruejo, C. González, J. LLorca, Ballistic performance of hybrid nonwoven/woven polyethylene fabric shields, International Journal of Impact Engineering, 2018;vol. 111: pp. 55-65.

[29] R. Muñoz, F. Martínez-Hergueta, F. Gálvez, C. González, J. LLorca, Ballistic performance of hybrid 3D woven composites: Experiments and simulations, Composite Structures, 2015;vol. 127:pp. 141-151.

[30] A. García-Carpintero, M. Herráez, J. Xu1, C. S. Lopes, C. González, A Multi Material

Shell Model for the Mechanical Analysis of Triaxial Braided Composites, 2017.

Figure captions

Tables

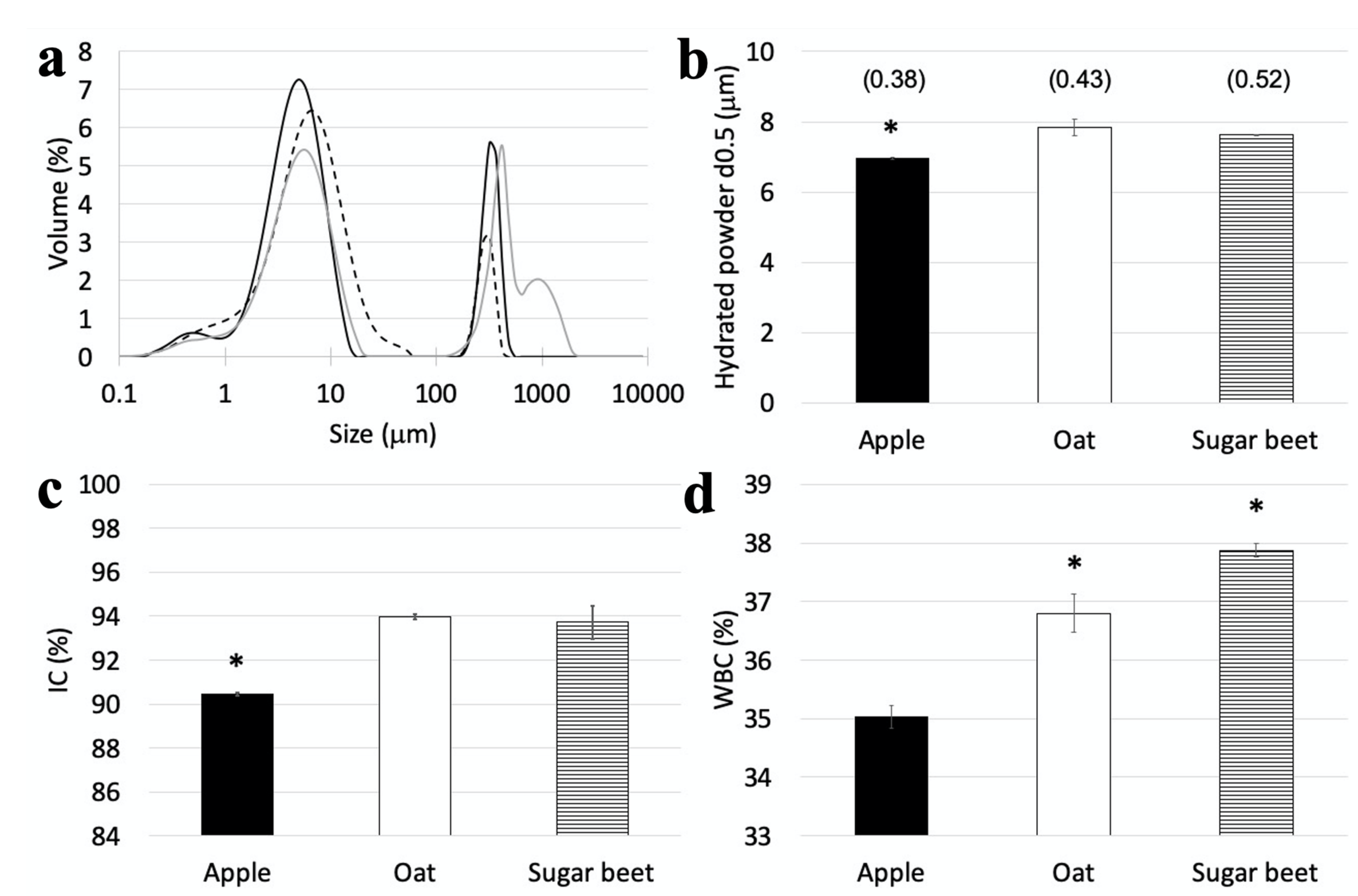
a
Volume (%)
0
1
2
3
4
5
6
7
8
0.1
1
10
100
1000
10000
Size (µm)
b
Hydrated powder d0.5 (µm)
0
2
4
6
8
10
(0.38)
(0.43)
(0.52)
*
Apple
Oat
Sugar beet
c
IC (%)
84
86
88
90
92
94
96
98
100
*
Apple
Oat
Sugar beet
d
WBC (%)
33
34
35
36
37
38
39
*
*
*
Apple
Oat
Sugar beet

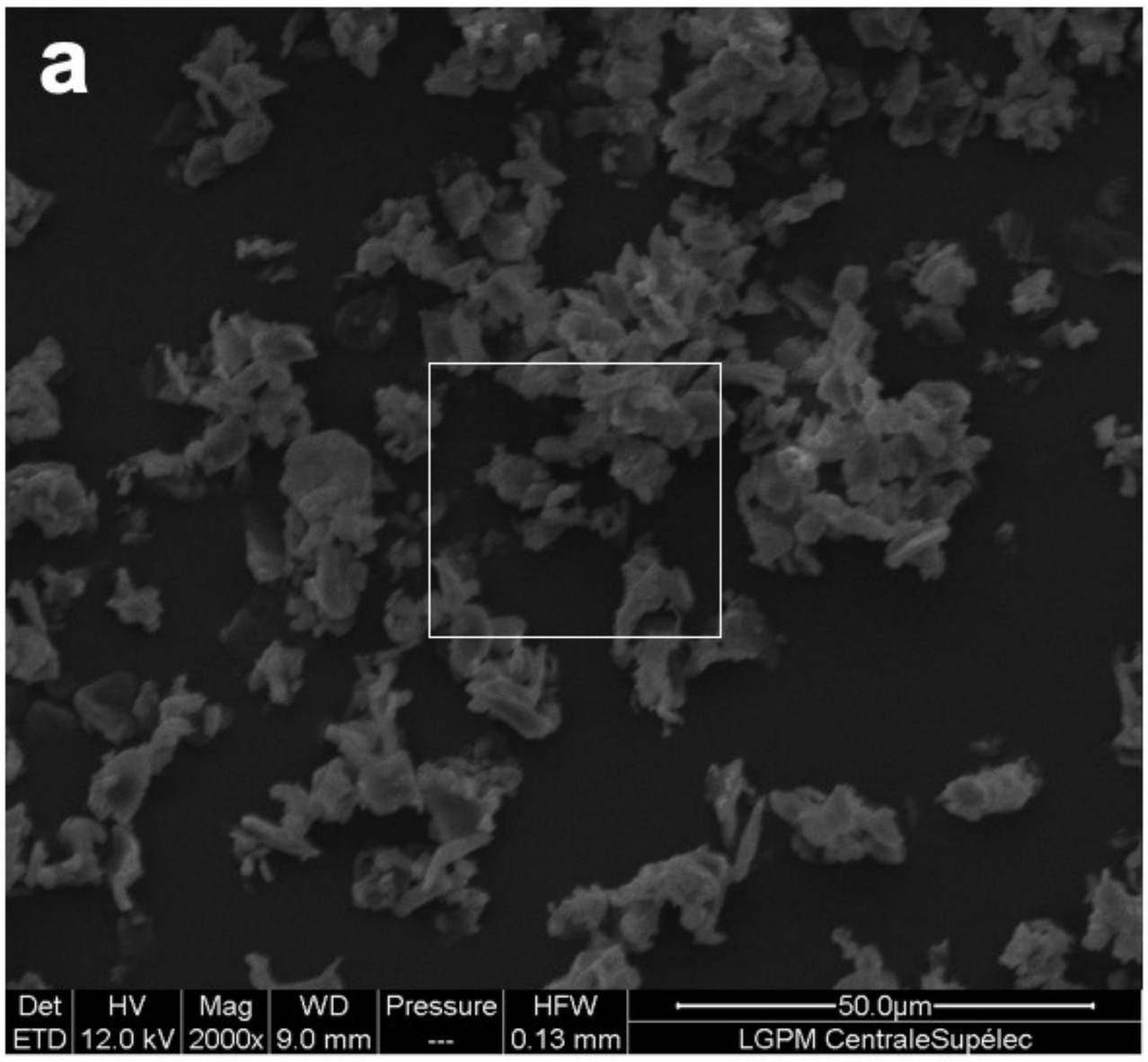
a
Det HV Mag WD Pressure HFW
ETD 12.0 kV 2000x 9.0 mm --- 0.13 mm
50.0µm
LGPM CentraleSupélec

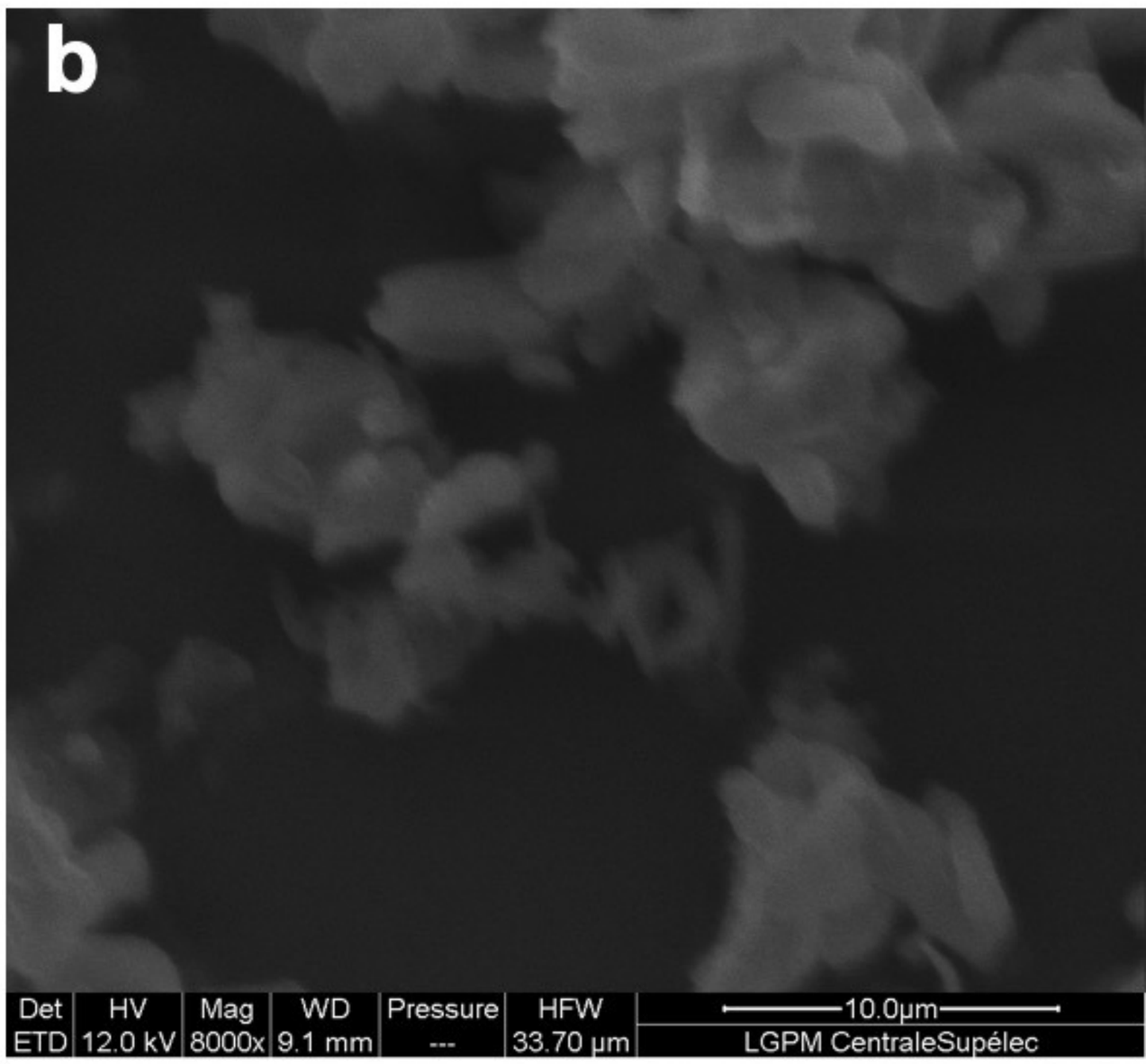
b
Det HV Mag WD Pressure HFW
ETD 12.0 kV 8000x 9.1 mm --- 33.70 µm
10.0µm
LGPM CentraleSupélec

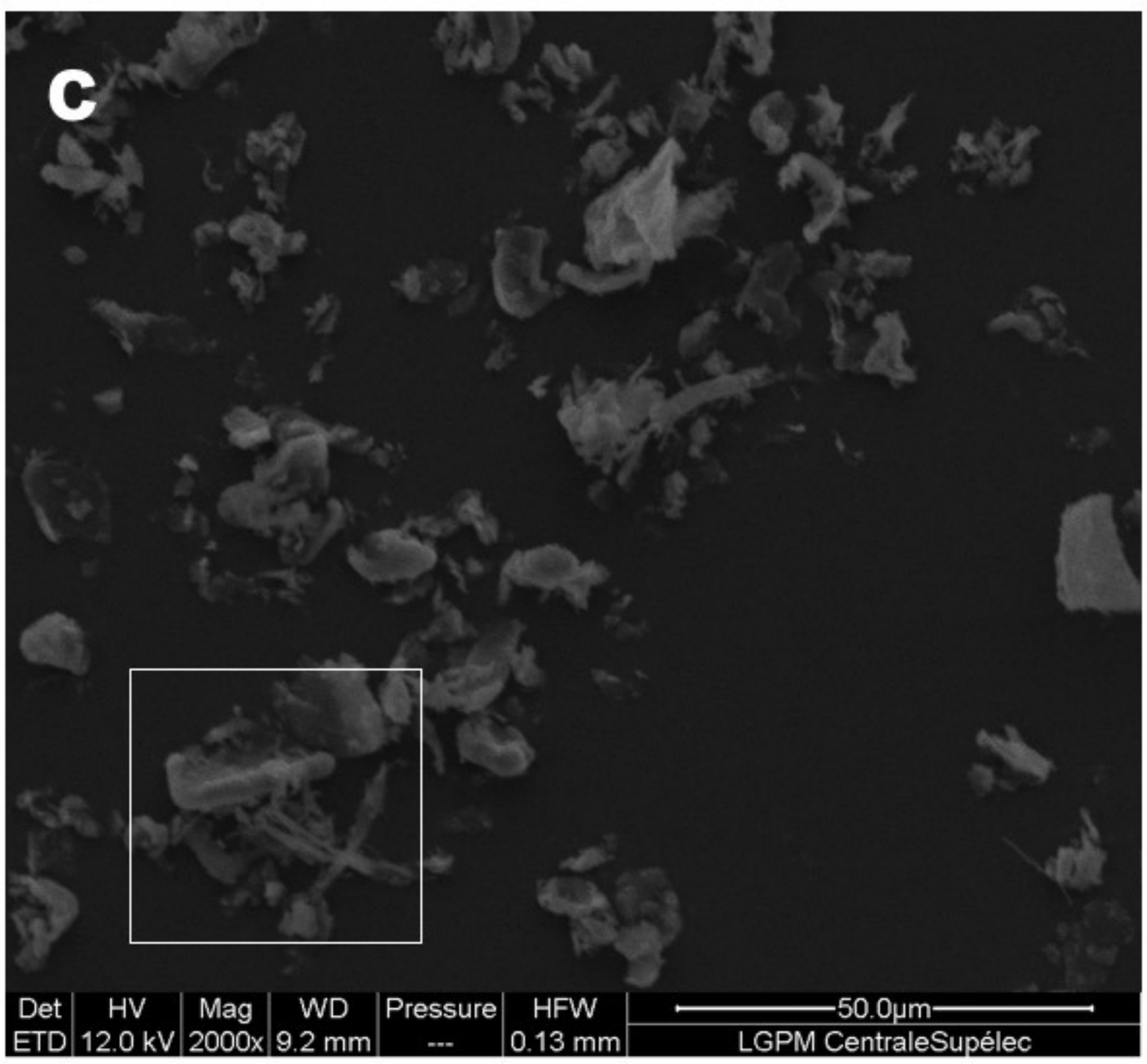
c
Det HV Mag WD Pressure HFW
ETD 12.0 kV 2000x 9.2 mm --- 0.13 mm
50.0µm
LGPM CentraleSupélec

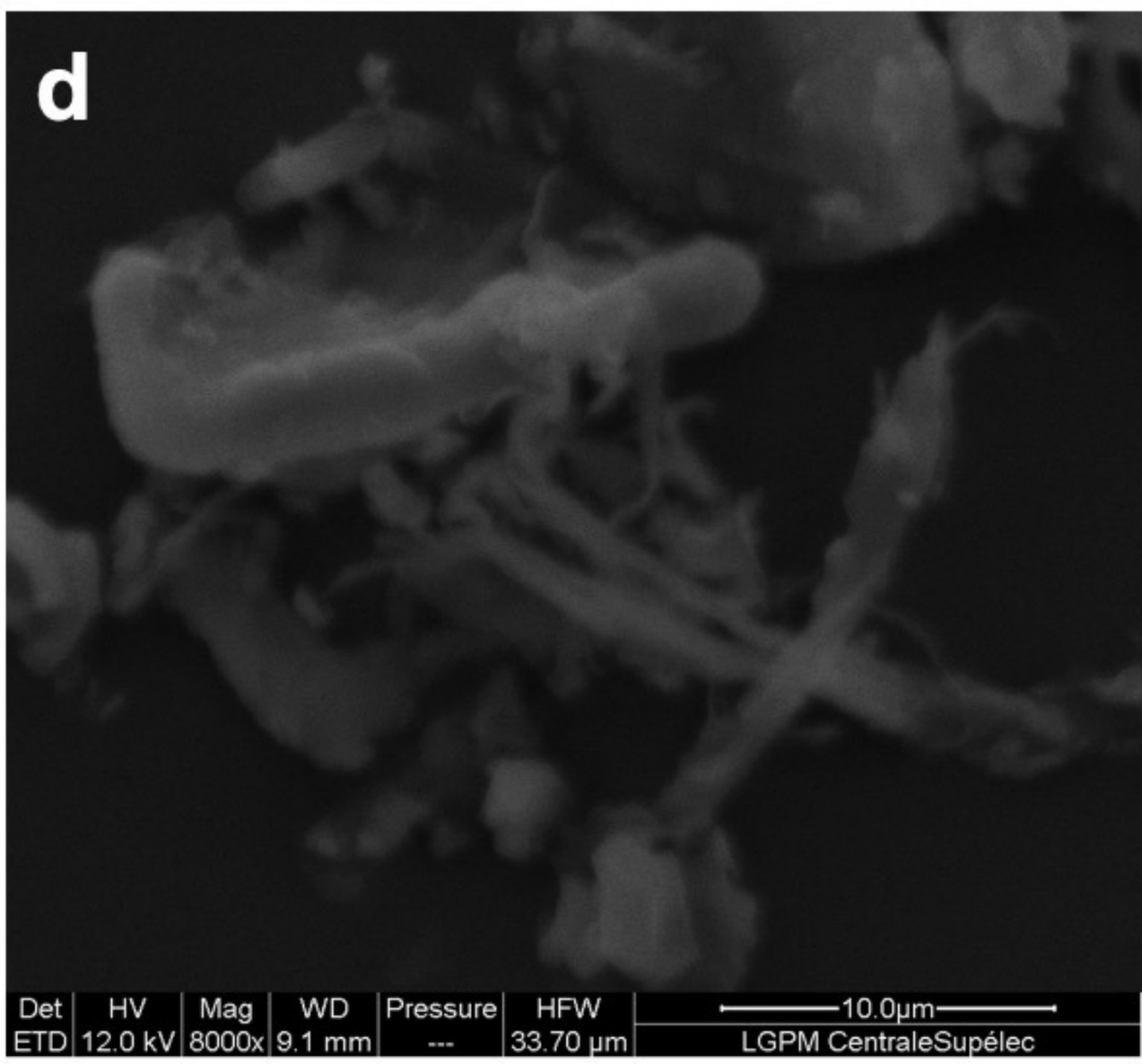
d
Det HV Mag WD Pressure HFW
ETD 12.0 kV 8000x 9.1 mm --- 33.70 µm
10.0µm
LGPM CentraleSupélec

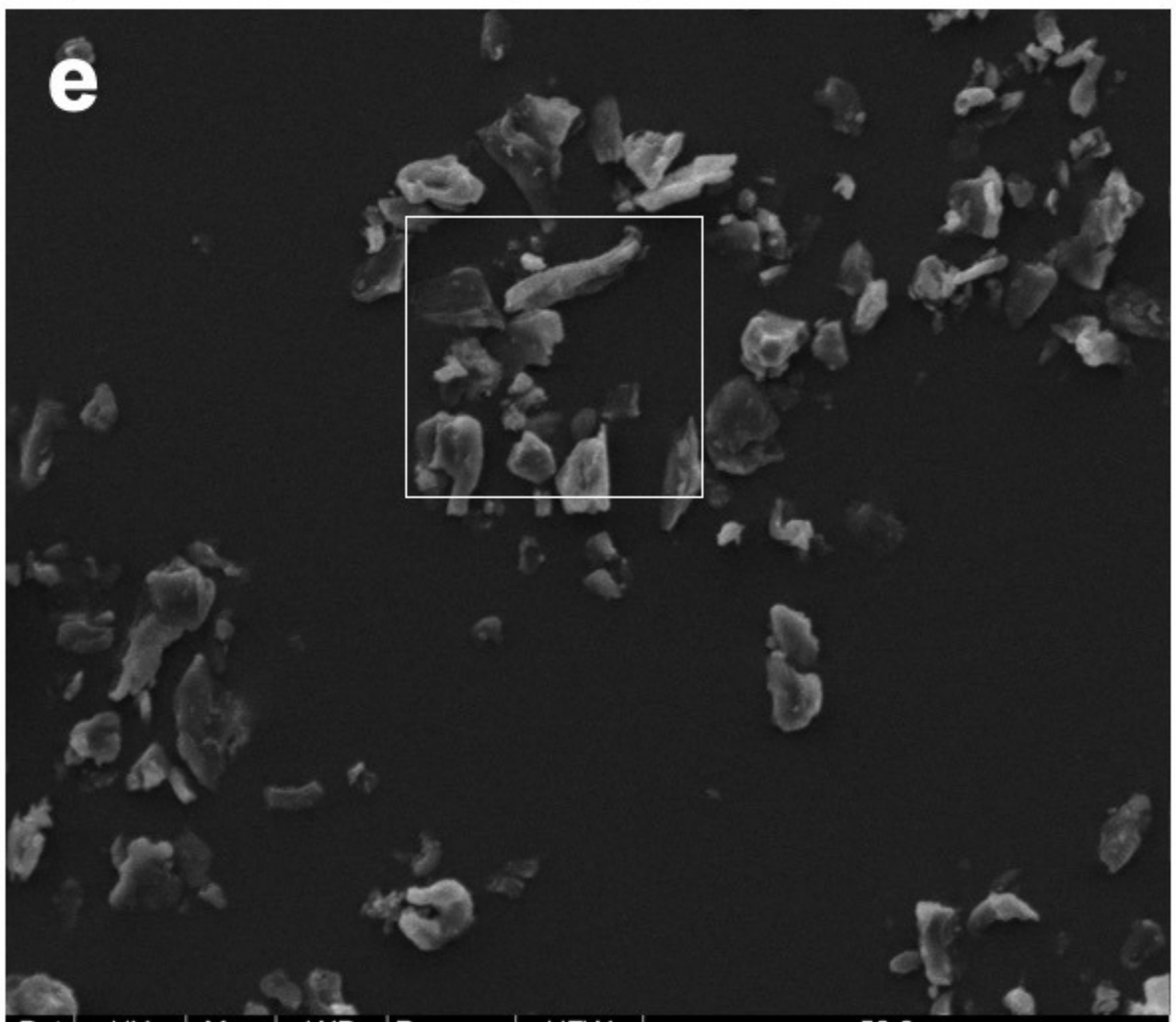
e
Det HV Mag WD Pressure HFW
ETD 12.0 kV 2000x 9.1 mm --- 0.13 mm
50.0µm
LGPM CentraleSupélec

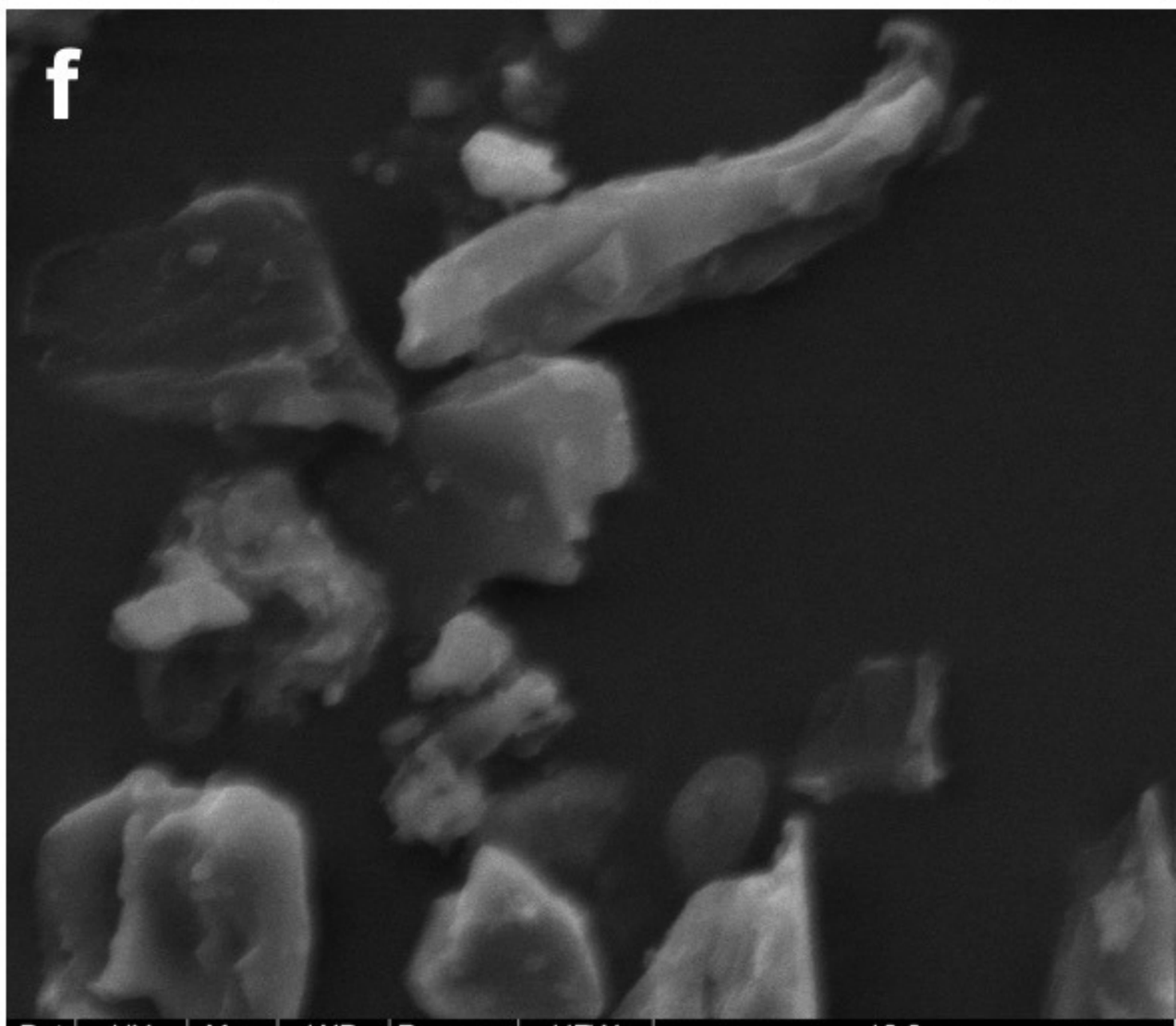
f
Det HV Mag WD Pressure HFW
ETD 12.0 kV 8000x 9.1 mm --- 33.70 µm
10.0µm
LGPM CentraleSupélec

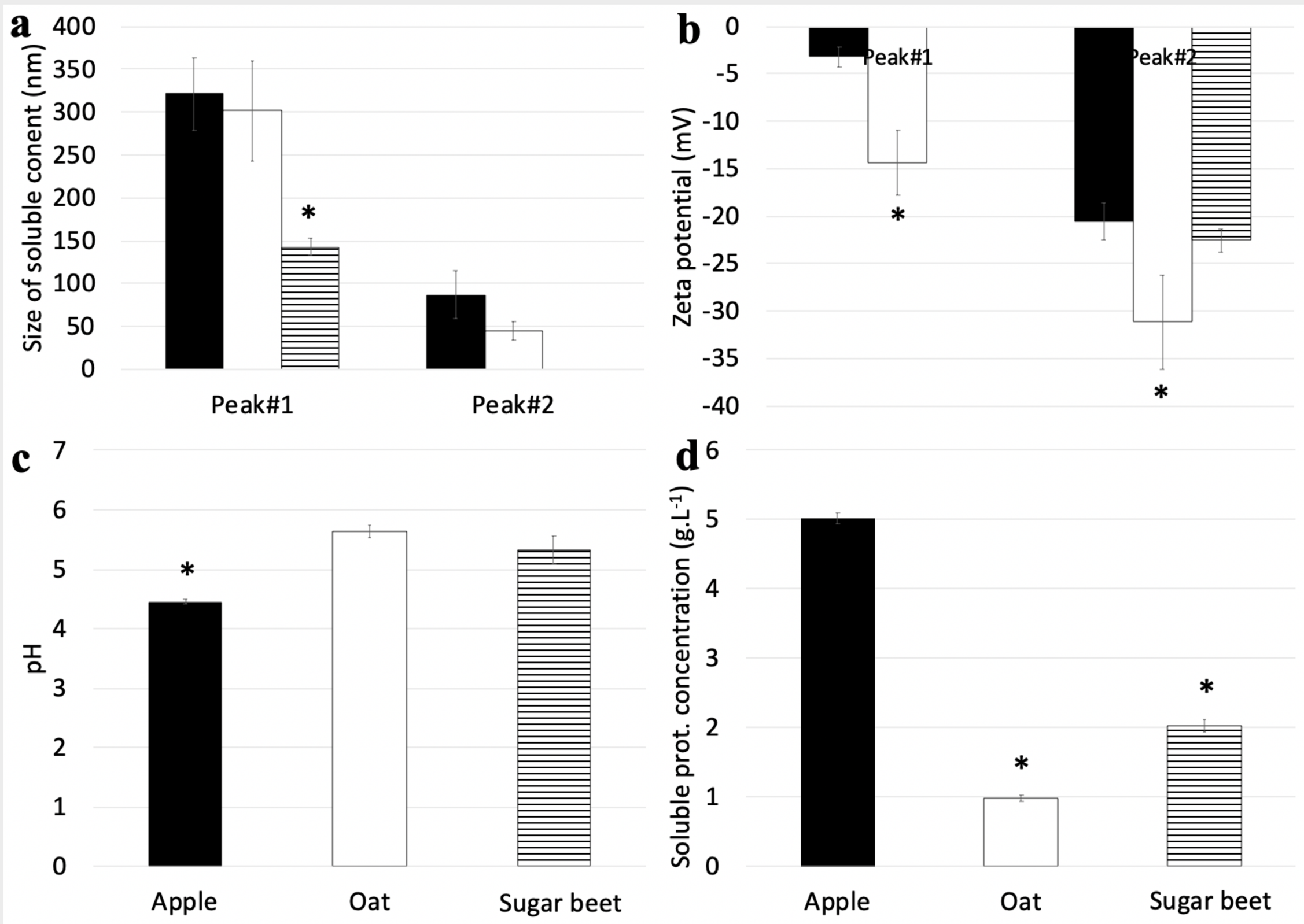
a
Size of soluble conent (nm)
400
350
300
250
200
150
100
50
0
*
Peak#1
Peak#2
b
Zeta potential (mV)
0
-5
-10
-15
-20
-25
-30
-35
-40
Peak#1
Peak#2
*
*
c
pH
7
6
5
4
3
2
1
0
*
Apple
Oat
Sugar beet
d
Soluble prot. concentration (g.L-1)
6
5
4
3
2
1
0
*
*
Apple
Oat
Sugar beet

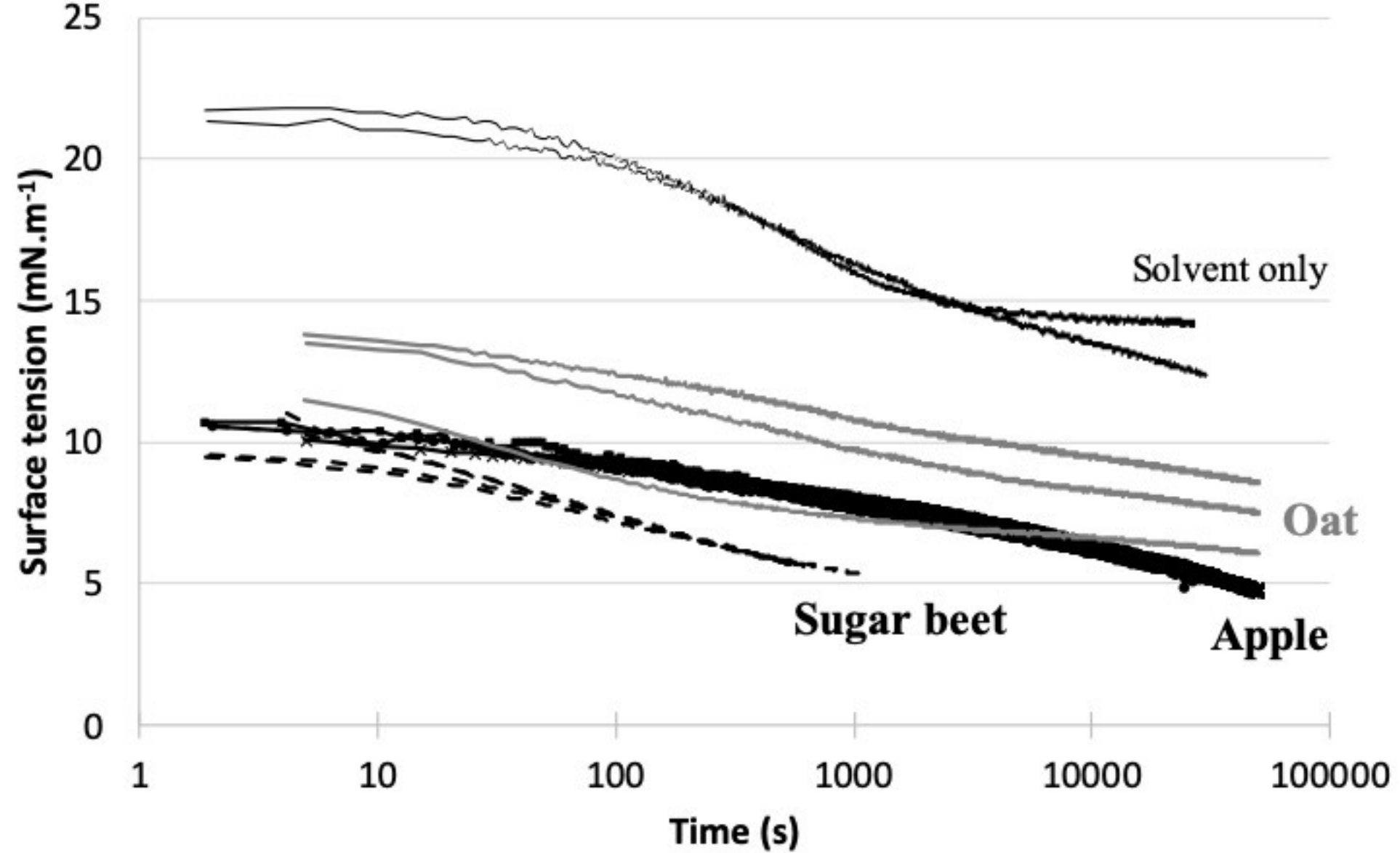
25
20
15
10
5
0
Surface tension (mN.m-1)
1
10
100
1000
10000
100000
Time (s)
Solvent only
Oat
Sugar beet
Apple

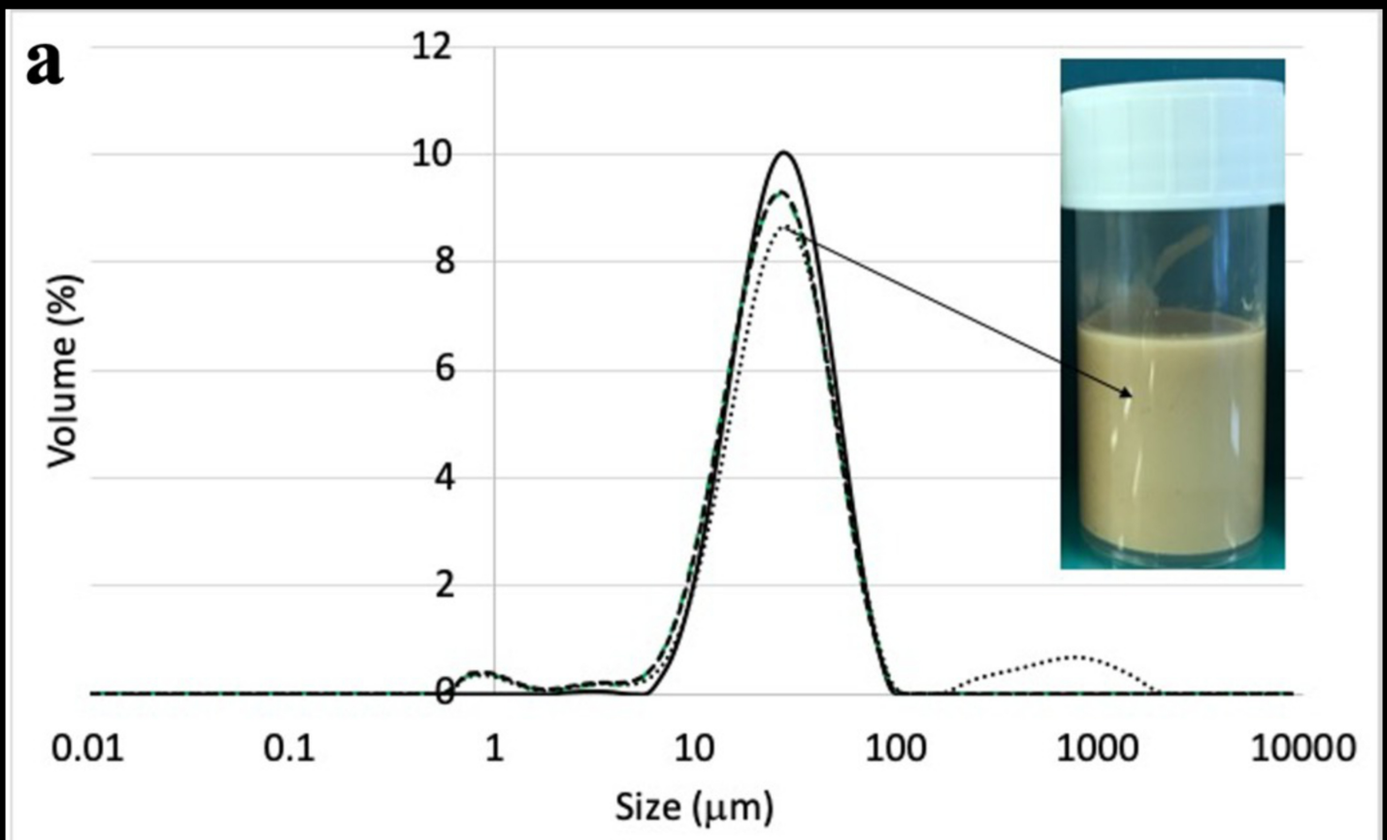
a
12
10
8
6
4
2
0
Volume (%)
0.01
0.1
1
10
100
1000
10000
Size (µm)

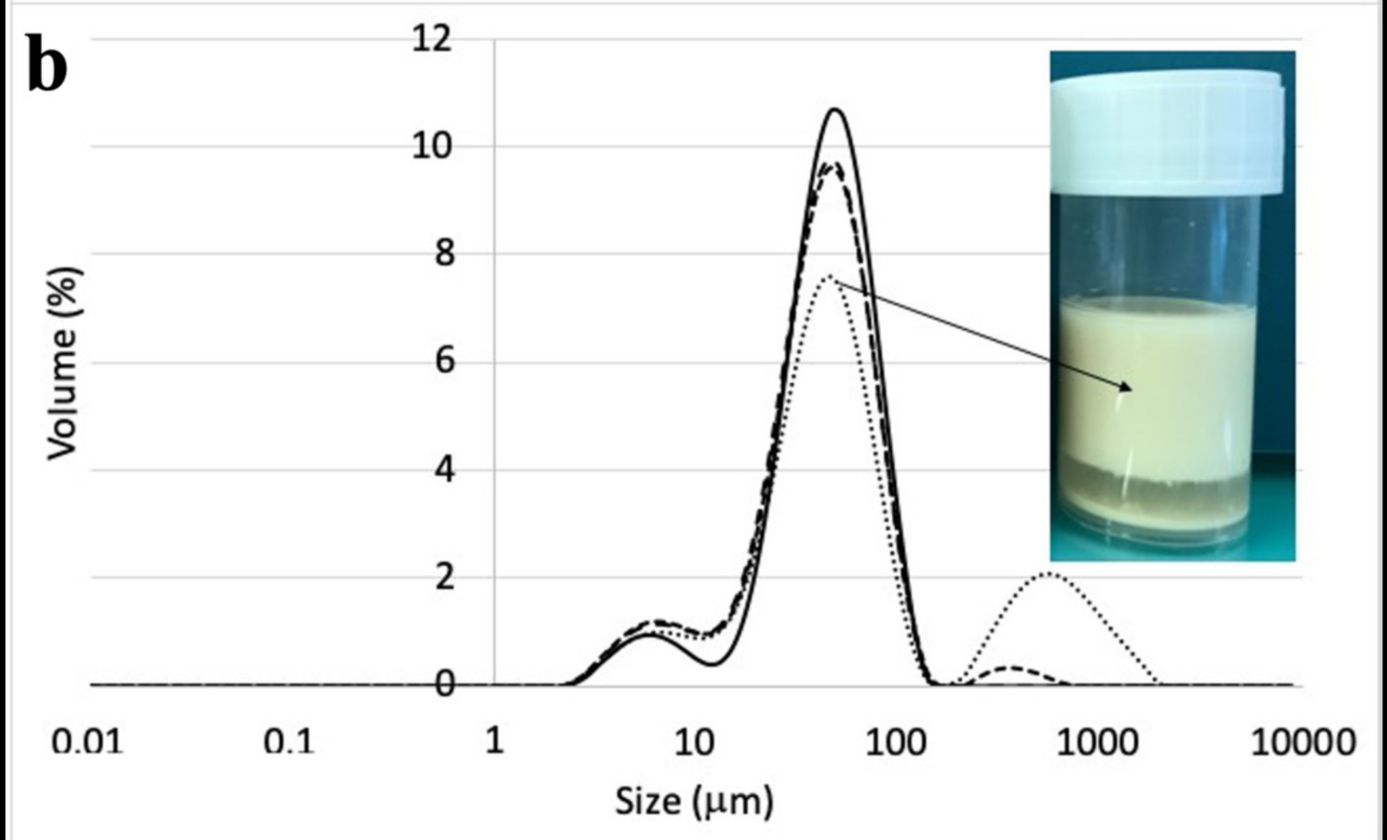
b
12
10
8
6
4
2
0
Volume (%)
0.01
0.1
1
10
100
1000
10000
Size (µm)

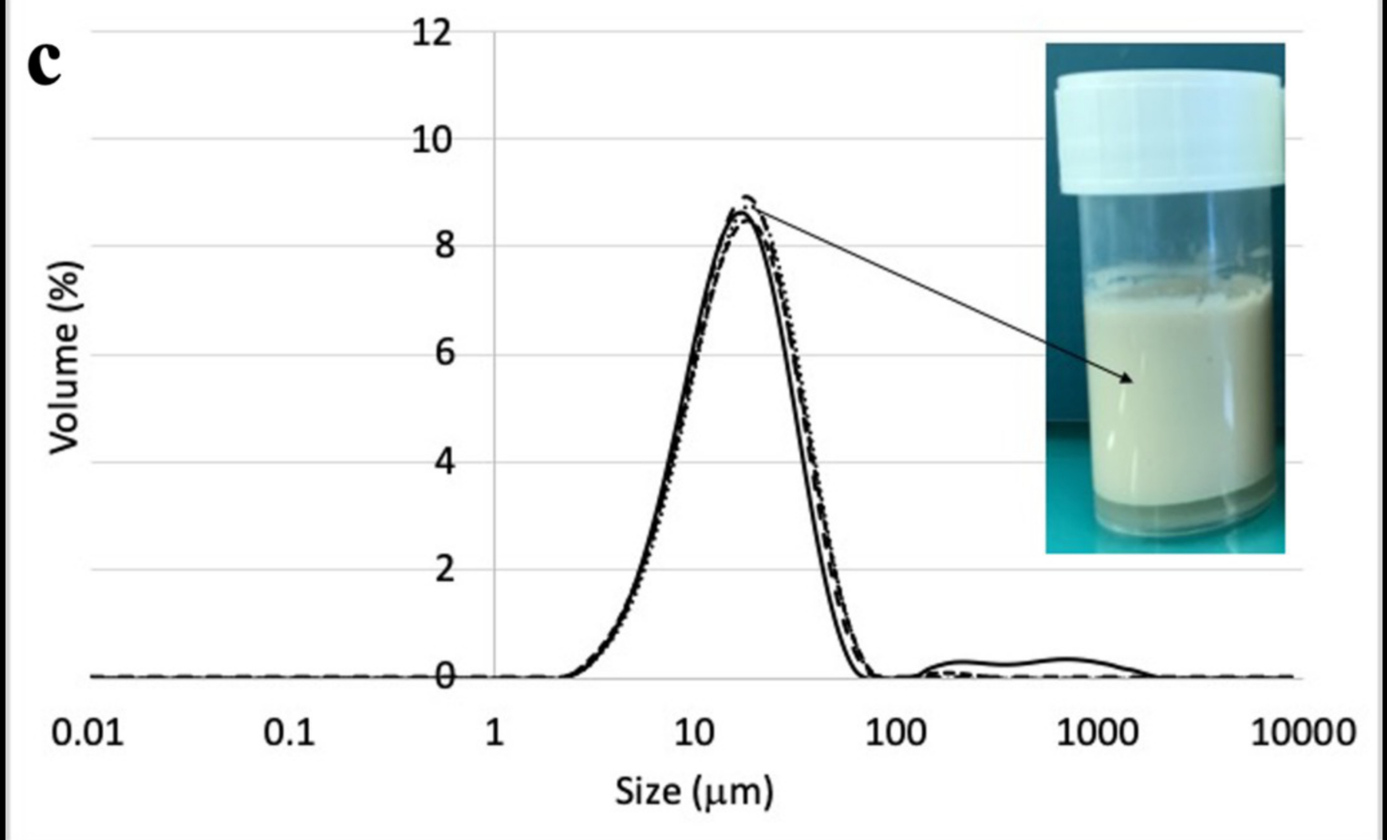
c
12
10
8
6
4
2
0
Volume (%)
0.01
0.1
1
10
100
1000
10000
Size (µm)

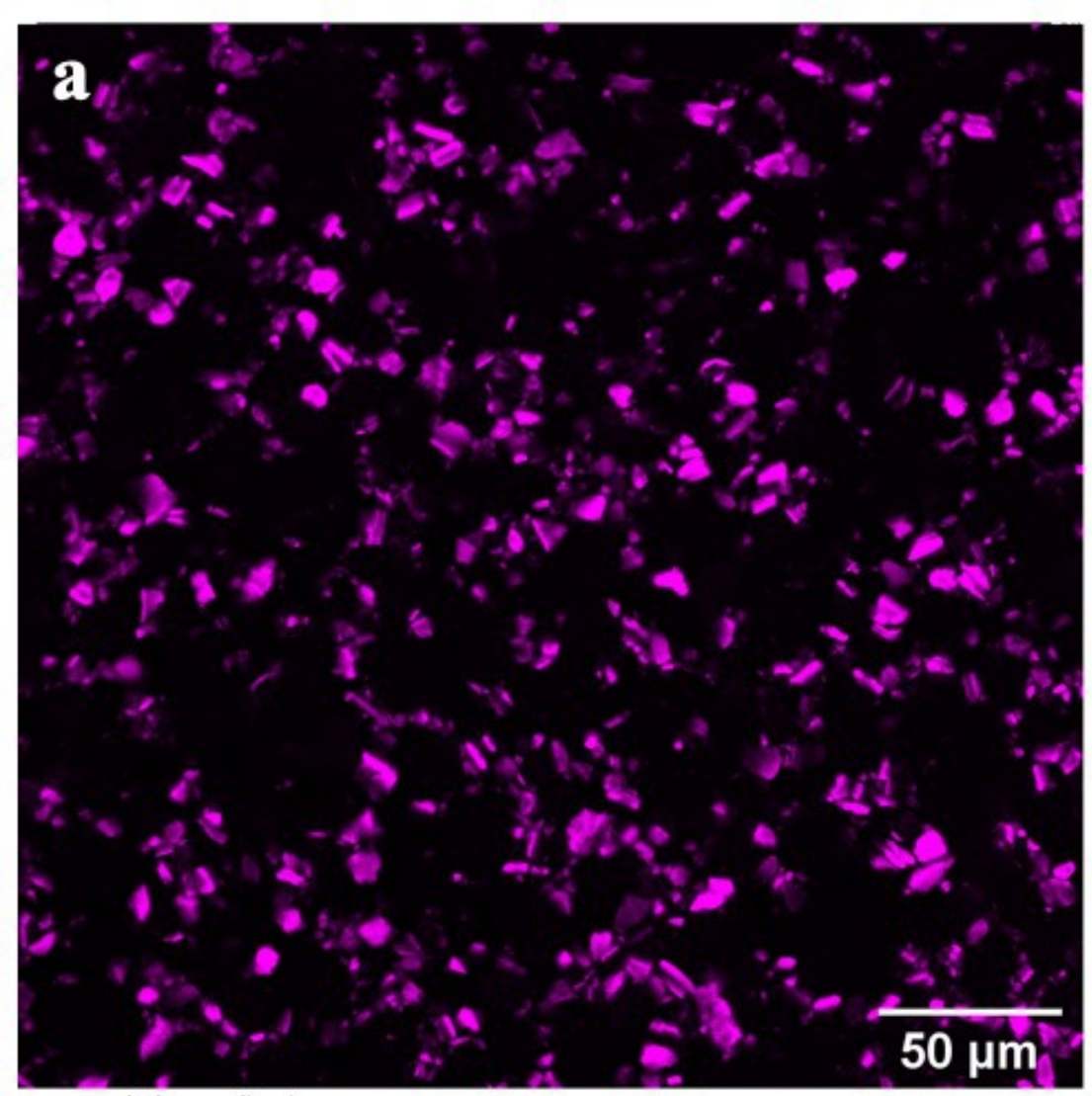
a
50 μm

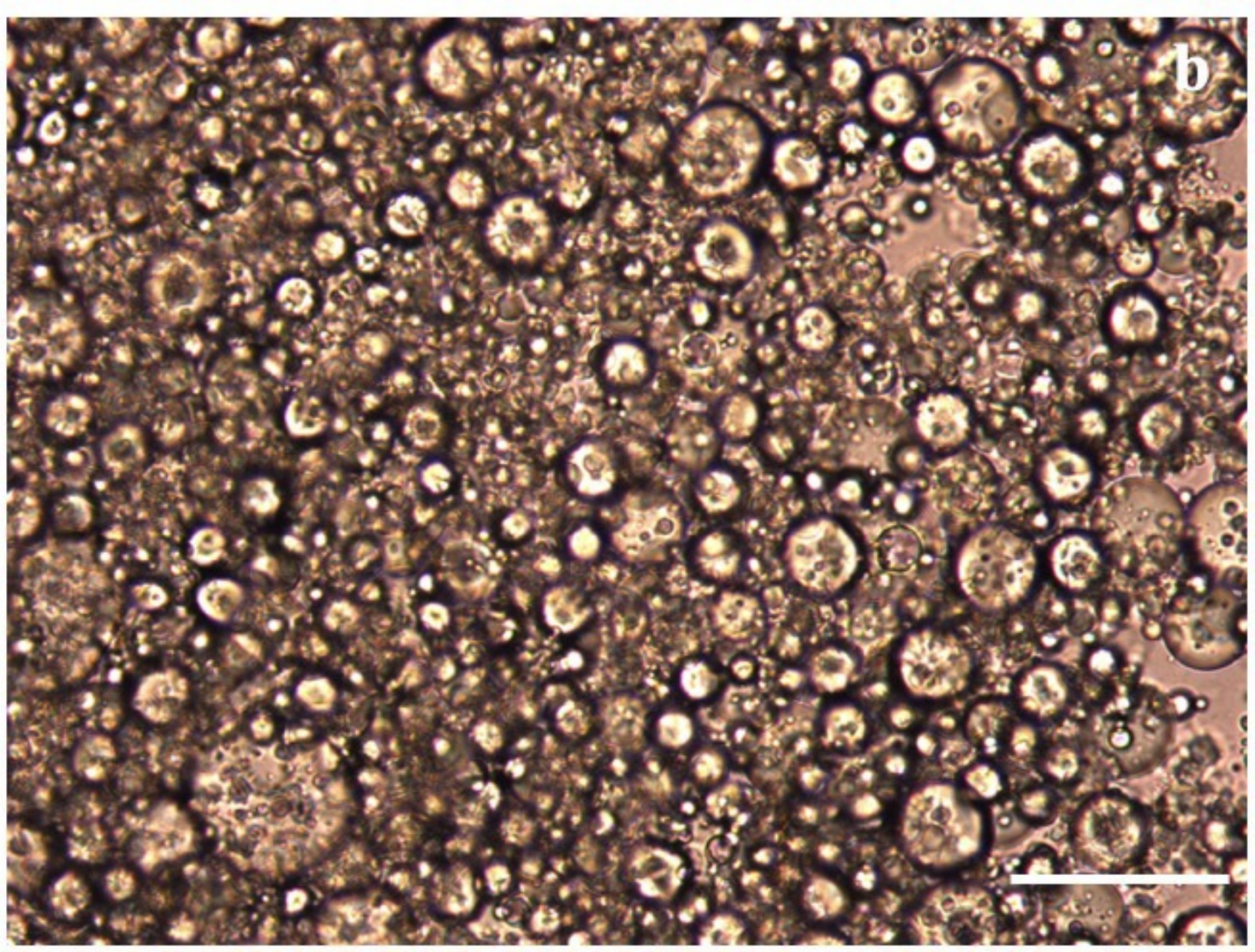
b

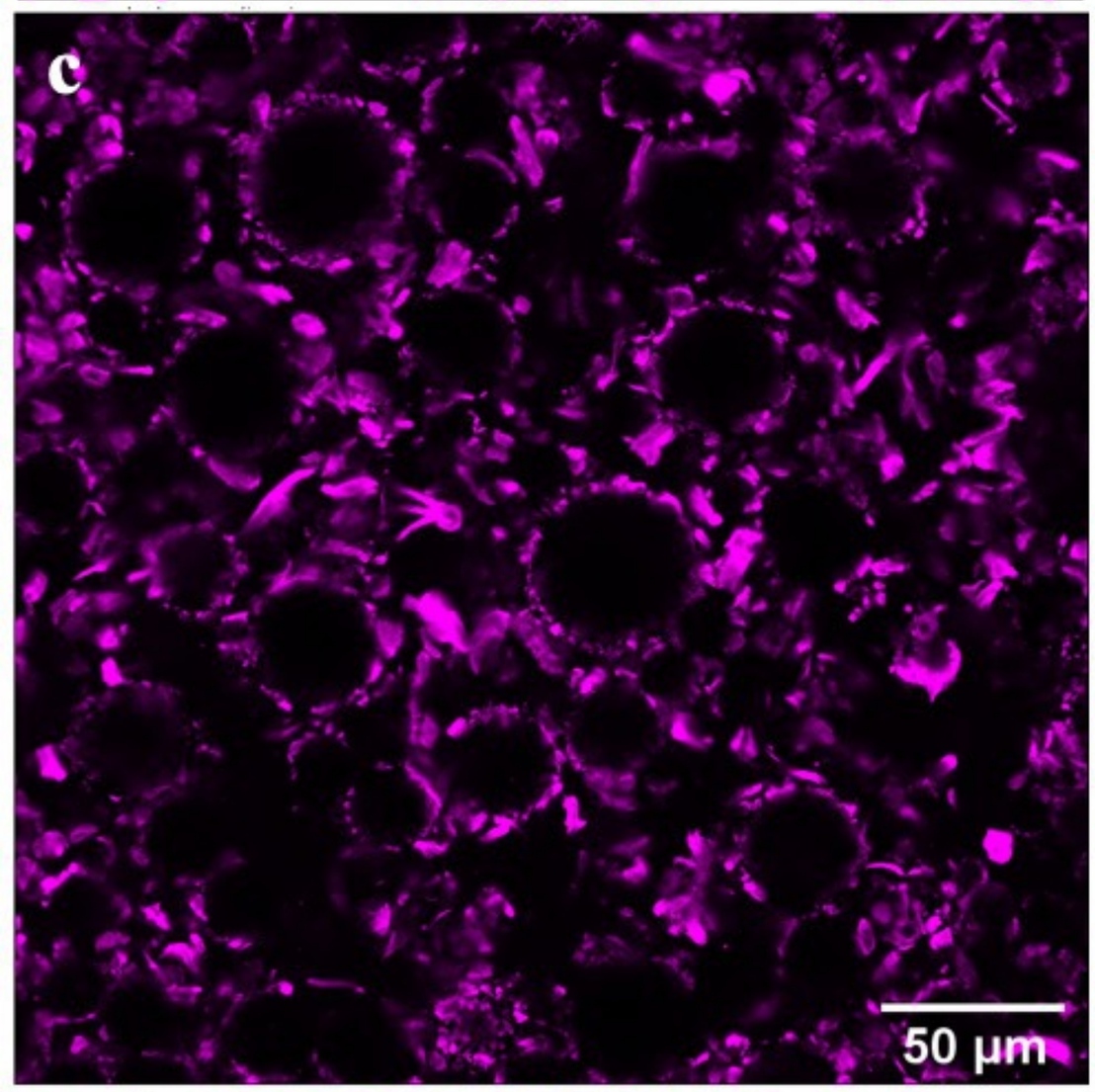
c
50 μm

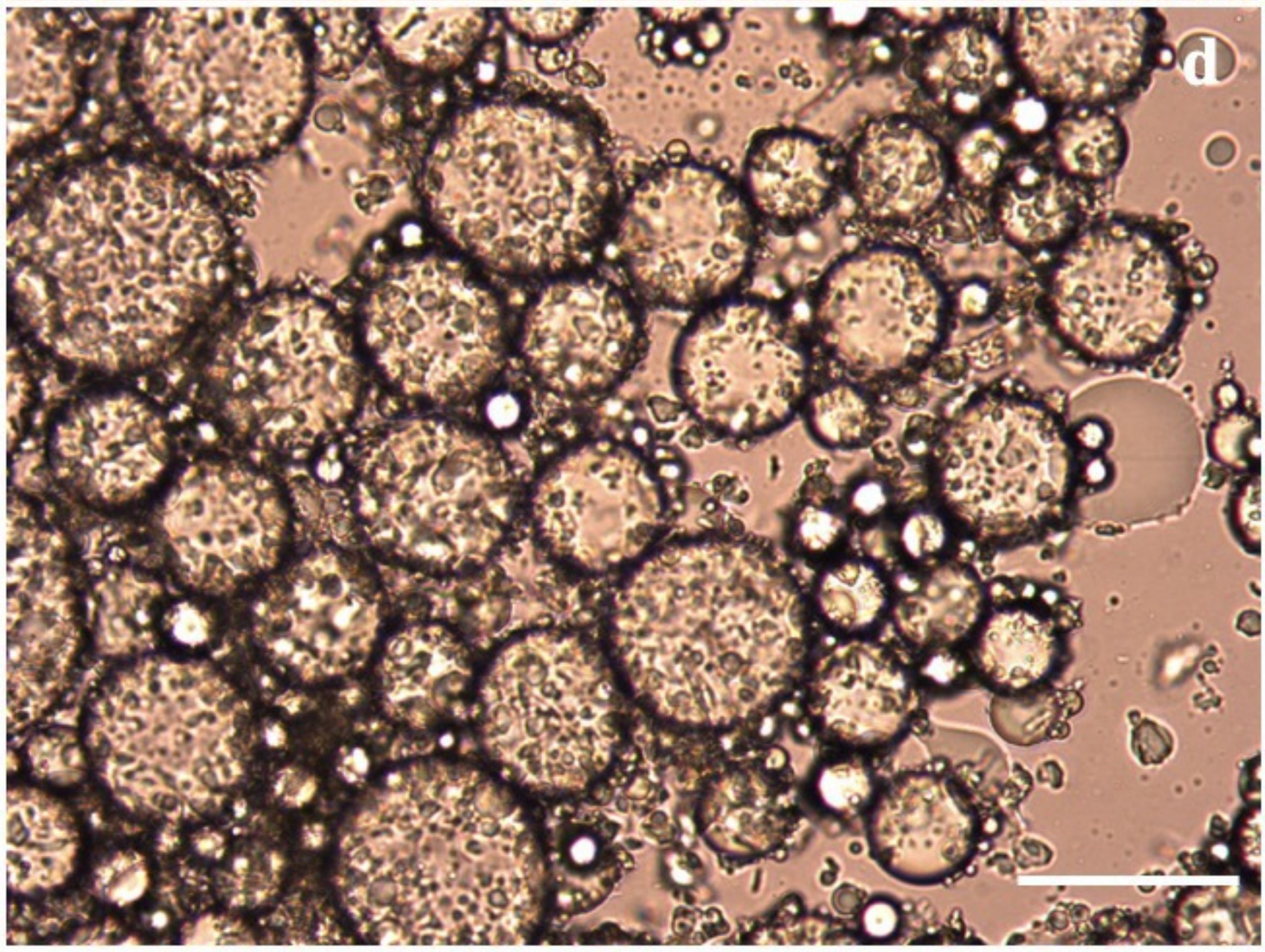
d

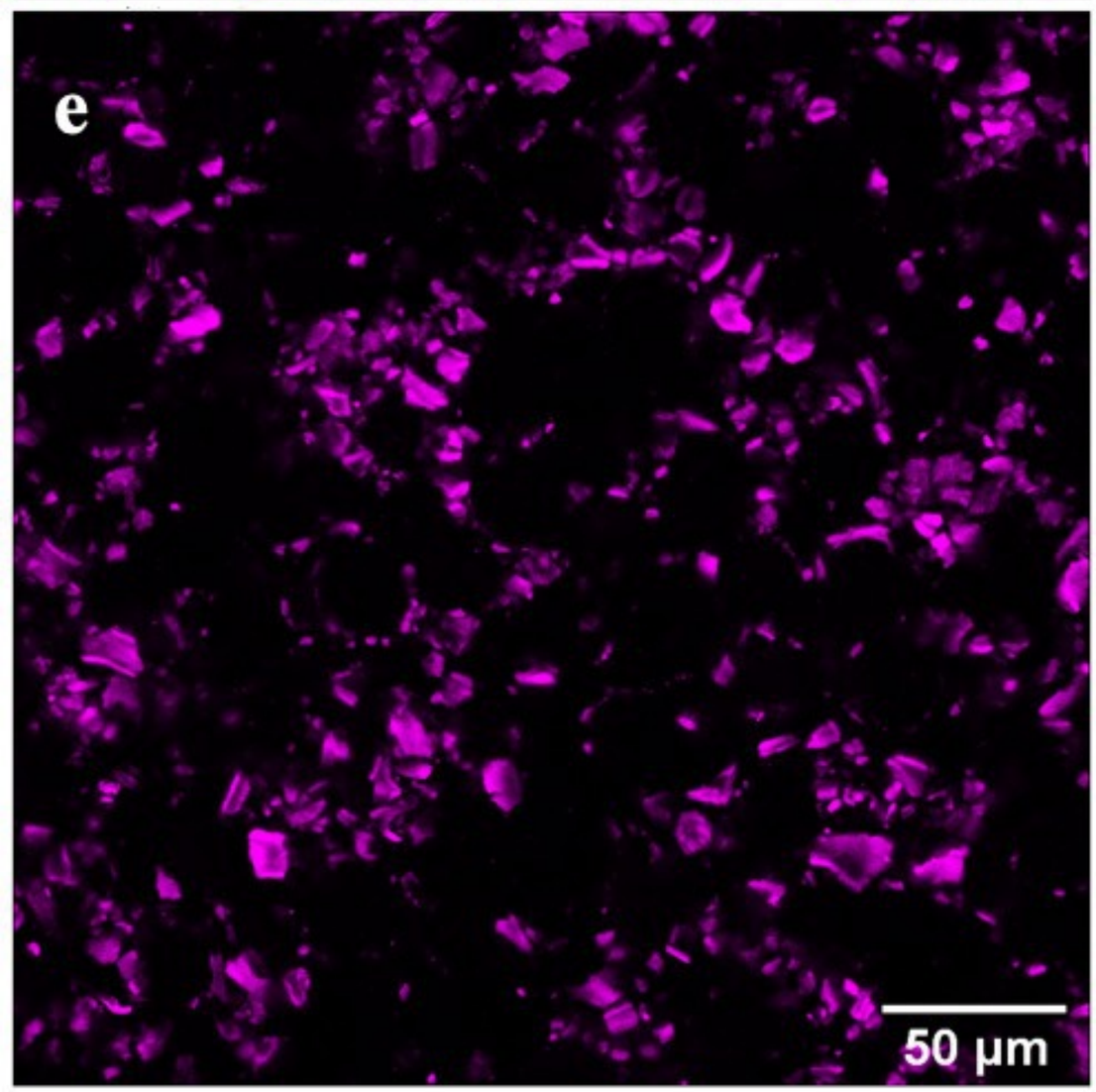
e
50 μm

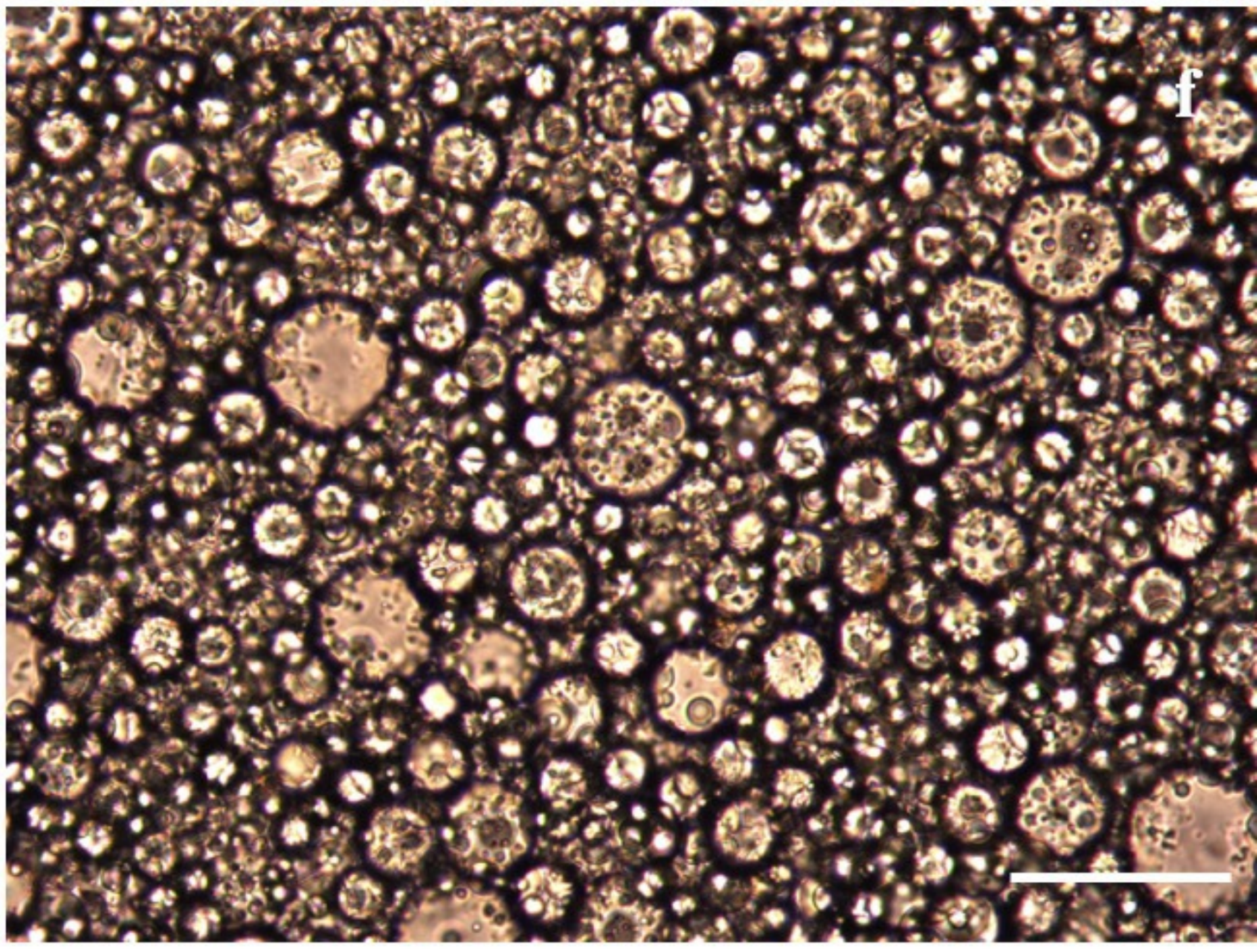
f

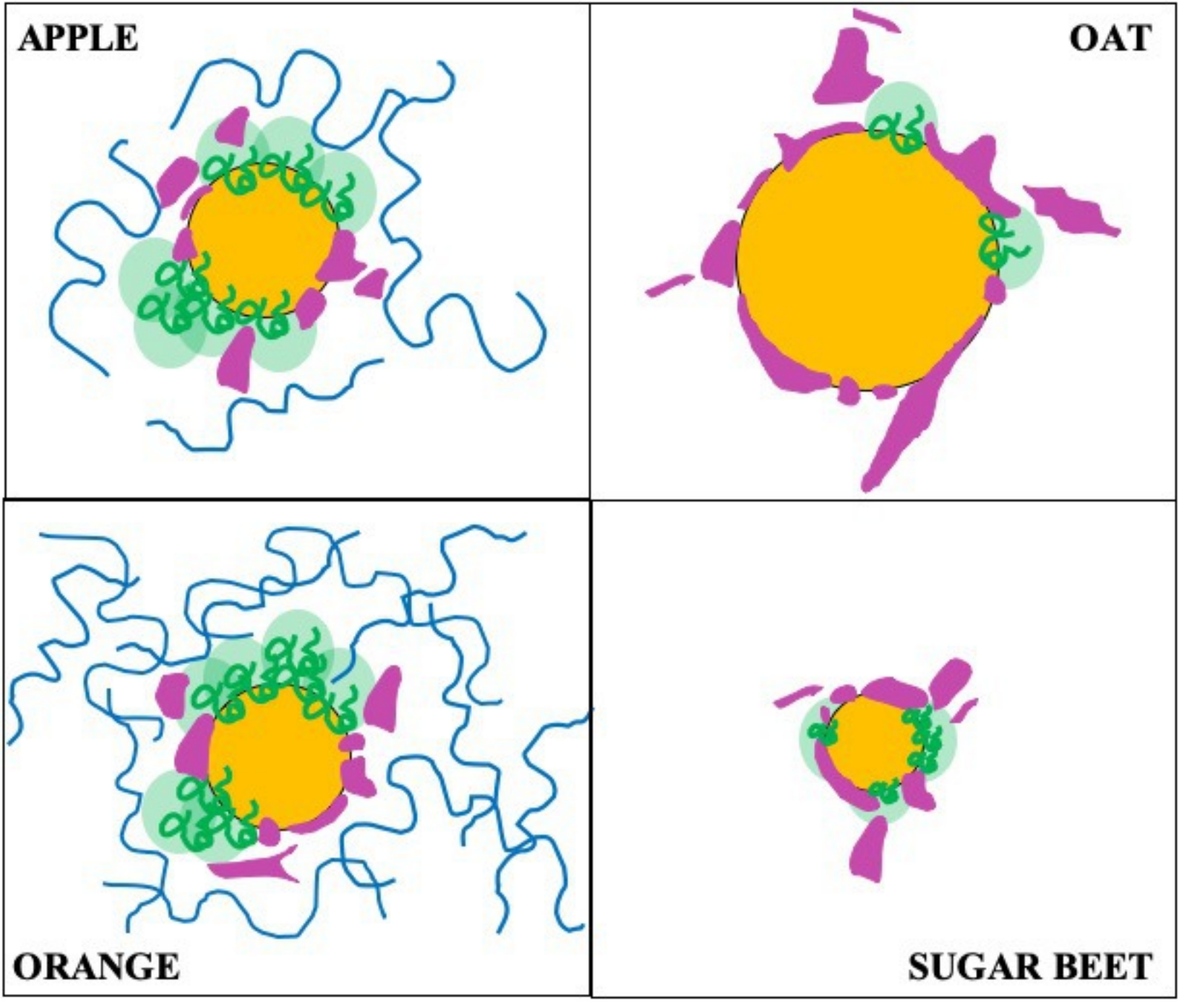
APPLE
OAT
ORANGE
SUGAR BEET

Particles	Modifications	Oil phase	Particles load	Emuls. vol.	Emulsification	Drop. size (μm)	Storage	Reference
Starch (rice, potato, wheat)	Precipitation, fractionation and OSA (potato) // heating (other sources)	50% vol (corn & anisole oil)	5 %wt	4 mL	Vortex mixer 1 min	130 - 300	24 hours	[36]
Cocoa	Defatting	10 - 50%wt (sunflower)	0.5 - 12 %wt	20g	Turrax, US, microfluidization pressure	5	30 days	[20]
Amorphous cellulose	Phosphoric acid, centrifugation, cleaning	20% (dodecane)	0.07 - 1.11 % w/v	20mL	Dispersion 10,000 rpm 3 min	20 - 30	7 days	[15]
Starch (rice, maize, potato, wheat)	Native	50% (paraffin)	15%wt	14mL	Dispersion 10,000 rpm 4 min	> 190	2 months	[18]
Starch (rice, maize, potato, wheat)	OSA & spherulites	30% (orange oil)	3% w/v	?	Dispersion 20,000 rpm 2 min	14 - 35	30 days	[6]
Maize starch	Milling (MiniSeries machine) for 25h	30, 40 or 50% vol (soy bean oil)	2.4 ; 7.2 or 10%wt	?	Turrax (13,000 rpm; 3 min)	10 - 900	24 hours	[38]
SigmaCell cellulose Type 20	Milling (MiniSeries machine) for 15h	30 or 60% vol (MCT oil)	0.2 - 3.7 %	?	Turrax (10,000 rpm; 3 min)	40 - 70	24 hours & 1 month	[37]
Quinoa starch	on of granules from quion	27 - 84% (mygliol, paraffin & peanut)	39 - 214 mg/g oil	14mL	Vortex	15 - 74	2 months	[8]
Starch (sourcing?)	OSA	60 - 81,5% (paraffin, Tegosoft)	7.1 - 25% w/v	?	Turrax (9,600 - 22,000 rpm, 20 - 300 s)	80 - 140	3 months	[7]
Starch (quinoa, maize, oat)	OSA	5% MCT oil (mygliol 812)	200 - 1769 mg/ g oil	7 mL	Vortex 10 s + high-shear 22,000 rpm 1, 3 or 5 min	10 - 80	no storage	[9]
Quinoa starch	Extraction of granules from quiona + OSA	7 ou 10% (paraffine, MCT)	214 - 600 mg/mL oil	3mL	Dispersion 22,000 rpm 30s	30 - 45	2 months	[10]
Rice startch	OSA	16 - 75% (soy bean oil)	50 - 247 mg/mL oil	100 - 200 mL	Dispersion 11,000 rpm 2min	6 - 40	35 days	[11]
Quinoa starch	Extraction of granules from quiona + OSA	12.5 - 33.3%	12 - 1200 mg/mL oil	7mL	Dispersion 22,000 rpm 30s	20 - 65	1 day	[12]
Starch (various sources)	OSA or hydrophobic modification	20% (tetradecane)	1 - 3%wt	?	HPH 300 bar	0.8 - 13	?	[13]

Emulsion only stabilized by food byproduct powder

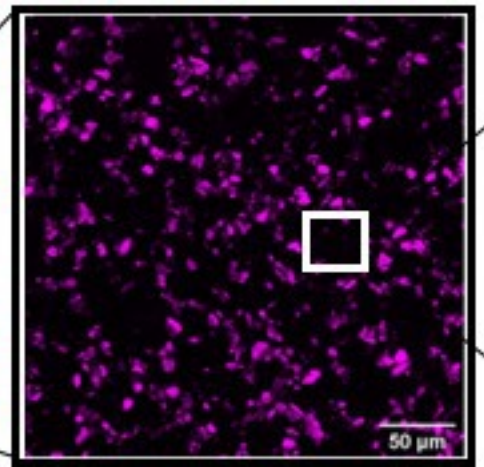

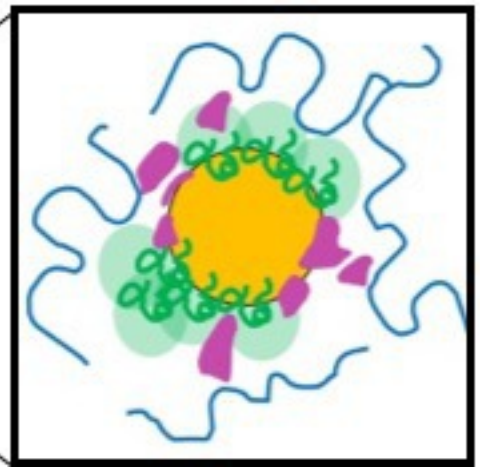

Oil
Particles
Soluble proteins
Polymers
Charges